OPTICAL AND DIELECTRIC PROPERTIES

OF ZnO NANOSTRUCTURES AT

TERAHERTZ FREQUENCIES

By

SANITH RAY

Bachelor Of Engineering

Sikkim Manipal University

Sikkim, India

2001

Submitted to the faculty
of the Graduate College of the
Oklahoma State University
in partial fulfillment
of the requirements
for the Degree of
MASTER OF SCIENCE
May, 2006

OPTICAL AND DIELECTRIC PROPERTIES

OF ZnO NANOSTRUCTURES AT

TERAHERTZ FREQUENCIES

Thesis Approved:

Dr. Weili Zhang
Thesis Advisor

Dr. Alan Cheville

Dr. Daniel Grischkowsky

A. Gordon Emslie
Dean of the Graduate College

ACKNOWLEDGEMENTS

First of all I would like to thank Dr. Weili Zhang, my advisor whose immense support and innovative ideas made this work possible. I express my sincere gratitude to him for his guidance, suggestion and enlightening discussions throughout the course of this work. Special thanks are also expressed to Dr. Daniel R. Grischkowsky and Dr. Allan Cheville for their helpful advice.

I would also like to thank Abul K Azad for his constant support and helping me in all possible ways. He was always a great support to me. I would also like to thank J.G. Han for his help and guidance in theoretical fitting on the experimental data.

Finally, I would like to thank my wife for being very supportive and patient. She performed the very tedious work of proof reading. Lastly, I also thank my parents and sister for being a source of constant support and inspiration throughout my academic career.

TABLE OF CONTENTS

Chapter **Page**

LIST OF FIGURES

Figure **Page**

LIST OF SYMBOLS

Notations	Descriptions
Al	Aluminum
c	speed of light in vacuum
cm	centimeter
d_o	Distance between receiver and M_1
d_1	Distance between M_1 and M_2
d_2	Distance between M_2 and M_3
d_3	Distance between M_3 and M_4
d_4	Distance between M_4 and transmitter
e	Normalized electrical field (V/m)
$E_{in}(t)$	Amplitude of Incoming THz beam
$E_{sample}(t)$	Amplitude of THz beam at the receiver (with sample)
$E_{reference}(t)$	Amplitude of THz beam at the receiver (without sample)
eV	Electron Volt
f	Filling factor
f(1,2)	Focal lengths of parabolic mirrors (treated as lens)

i	$\sqrt{-1}$
mm	Millimeter
m^*	Effective mass of the electron
M(1,2,3,4)	Mirror naming
μm	Micrometer
N	Carrier density
nm	Nanometer
n_s and n_m	Refractive Index of sample and material
$n(\omega)$	**Co**mplex refractive Index
$n_r(\omega)$	Real part of refractive index
$n_i(\omega)$	Imaginary part of refractive index
t	Time (second)
$t_{sm,}$ $t_{ms,}$ $t_{sa,}$ t_{as}	Fresnel's coefficients
β	Phase Shift
λ	Wavelength
α	Absorption
$\bar{\varepsilon}^{MG}$	Effective dielectric permeability of the sample concerned
ε_m	Dielectric permeability of surrounding medium
ε_h	**D**ielectric permeability of host
ε_∞	High-frequency dielectric constant

ε_0	Free-space permittivity 8.854×10^{12} F/m
μ	Mobility
ω_p	Plasma frequency
γ	Carrier damping constant
$\omega_{TO\,j}$	Oscillator strength
Γ_j	Phonon damping constant
ω	Angular Frequency, rad/sec

CHAPTER I

INTRODUCTION

This thesis presents Terahertz time-domain spectroscopy (THz-TDS) characterization of frequency dependent optical and dielectric properties of structures of ZnO in the far infrared. Researches in the THz regime began came into effect in late 80's and early 90's which eventually gained its momentum with in depth investigation of theories and exploring different areas of application.

1.1 Why Study ZnO

This research is mainly inspired by the potential application of the ZnO nanostructures in the THz regime. The increase in surface area and the quantum confinement effects has made nanostructured materials quite distinct from their corresponding bulk form as far as electrical and optical properties are concerned. ZnO being a II-VI compound has a very wide range of applications in the infrared and far-infrared region. Having a wide band-gap of 3.6 eV with high exciton gain, and a large exciton binding energy of ~60 meV, ZnO semi-conductor is well known for having low-voltage and short-wavelength optoelectronics applications [1-3]. ZnO nanostructures are reported to have potential applications for piezoelectric transduction, optical emission, catalysis, actuation, drug delivery and optical storage with promising photoelectronic, photochemical and catalytic

properties [4]. High resistivity, high mobility (200 cm^2/Vs) and very less fabrication barrier makes ZnO an ideal choice for high power THz generation [5, 7]. Due to all these properties, ZnO remains an important material for applications in gas sensors, varistors, rubber additives, pigments and optical devices in both fundamental research and practical studies [6].

Besides, ZnO crystal is of great use as a photoconductive material for the generation of THz because of its ease in the fabrication process, wide band gap character and high mobility and resistivity. Further applications of ZnO crystals involves in its capacity to generate second harmonics of Ti:sapphire laser as its transmission edge is located at 390 nm. All these definitely make ZnO a suitable candidate to be used as a high power emitter [7].

1.2 Thesis Outline

Various structures of ZnO (tetrapods and nanowires) are characterized and analyzed using terahertz time-domain spectroscopy to investigate their low-frequency optical and dielectric properties. The power absorption and refractive index, as well as the complex dielectric function, were measured in the frequency range from 0.1 to 3.5 THz. Based on a simple effective medium theory, the low-frequency dielectric properties of ZnO structures are found to be associated with the transverse optical E_1 phonon mode, which corresponds well to that of the bulk ZnO.

Chapter 2 describes the THz system used to characterize the ZnO samples and the basic

structure of the cells containing them. Chapter 3 discusses in details about the data extrapolation steps used in this work. Chapter 4 describes in details about the related theories while chapter 5 describes the analysis steps and results obtained for each samples. Then chapter 6 summaries the whole thesis and some potential future work are being included in chapter 7.

CHAPTER II

TERAHERTZ TIME DOMAIN SPECTROSCOPY AND CELL STRUCTURE

2.1 Basic THz-TDS system

Because of high signal to noise ratio (~10,000:1) and nonionizing properties, THz-TDS has been recognized as a preferable far-infrared spectroscopic approach [10]. The THz-TDS system used in this work is based on the principle of photoconductive switching. In this section the transmitter and the receiver systems are explained in detail.

Working Principle of the THz system

The Conventional Grischkowsky-type THz-TDS system is the basis of the modified 8-F confocal system used in this work. Fig 2-1 illustrates this basic system which shows distinctly the terahertz transmitter to generate THz, the receiver, and the collimating optics (a set of parabolic mirrors and silicon lenses) to guide the THz pulse. The terahertz radiation is first generated by a transmitter which is essentially made up of coplanar transmission lines of metals on GaAs wafer [11]. This transmitter system is shown in Fig 2-2 and described in following section [12]. This produces a THz beam which impinges on the silicon lens placed in front of the GaAs chip as shown in Fig 2-1 [11].

The THz beam thus produced is then guided by a set of parabolic mirrors which further collimates the beam on to a second silicon lens (receiver end) after which the THz beam falls on to the THz receiver made on SOS (Silicon-on-sapphire) wafer. This SOS wafer is also patterned (antenna structure) with metallic transmission lines with an antenna. The detailed geometry of the GaAs transmitter and the SOS receiver is discussed in the next section.

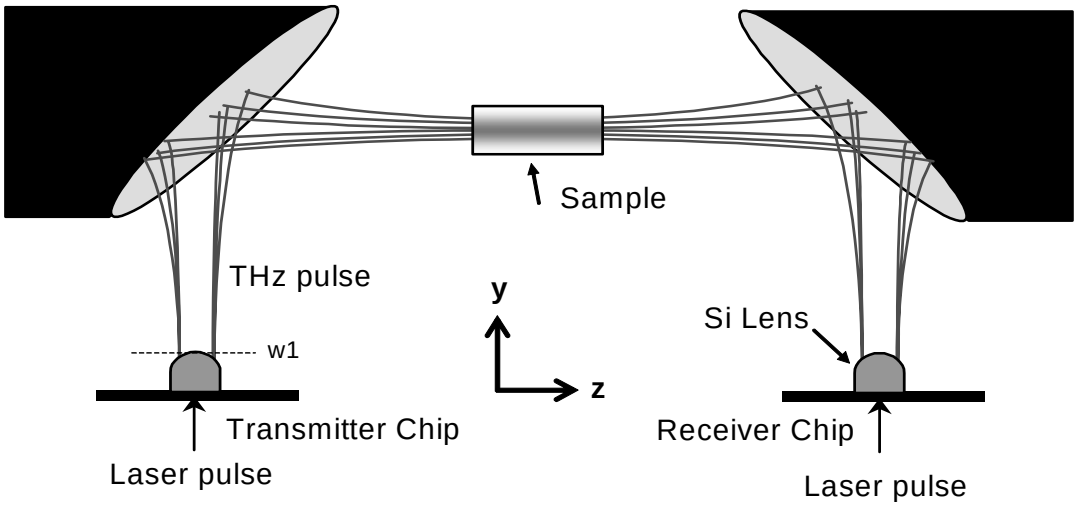

Figure 2-1: Experimental setup of standard THz system with two parabolic mirrors in 4-F confocal geometry (Focal lengths of the Mirrors are 11.9 cm). The sample shown is placed exactly in the midway between the parabolic mirrors.

THz transmitter and Receiver

The basic chip configurations of the THz transmitter and the receiver chips are shown below in Fig 2-2 and Fig 2-3 respectively [12]. This transmitter F-chip has coplanar transmissions lines made of two metals. The semi-insulating GaAs wafer is patterned in our class 1000 cleanroom facility and then electron beam evaporation technique is being employed to deposit a 100 nm thick titanium layer which is further metal coated with a 550 nm aluminum layer. As shown in the Fig 2-2 each transmission line are 10 μm thick and is separated by 80 μm [12].

In a very similar way our THz receiver chip is fabricated. As stated in the preceding section, our Max receiver chip patterned on a SOS wafer also consists of metal lines deposited by the same method of electron beam evaporation. These metal lines have a width of each 5 μm and separated from each other by 10μm. A dipole antenna gap of 5 μm is allowed between the lines [12]. The system configured with these above mentioned chips is able to generate a bandwidth up to 4.5 THz.

Working of the Chip

A 70 V of DC voltage is applied to bias the chip. This system is driven by a mode-locked Ti:Sapphire femtosecond pulse laser. Between the transmission lines of the transmitter chip a femtosecond laser is impinged [12,30]. This 800 nm femtosecond pulse causes a sub picosecond charge in between the lines causing a flow of electrical pulse in both directions of the transmission lines. The dark spot in the Fig 2-2 shows the focused impinged pulse. This impinged pulse generates an electron hole pair and the applied

biased voltage accelerates it thus to generate the THz pulses. The silicon lens which is placed exactly in front of the transmitter chip works together with the parabolic mirrors to collimate the THz beam. This beam is now focused by another silicon lens which allows it to fall on the antenna of the receiver chip. The configuration of the receiver chip as discussed earlier and shown in Fig 2-3 shows a black dot which is essentially the same focused femtosecond pulse from the Ti:sapphire laser but with a variable optical delay with the pulses on the transmitter. As the receiver is gated with the transmitter, a high signal-to-noise (~ 10000:1) ratio is obtained.

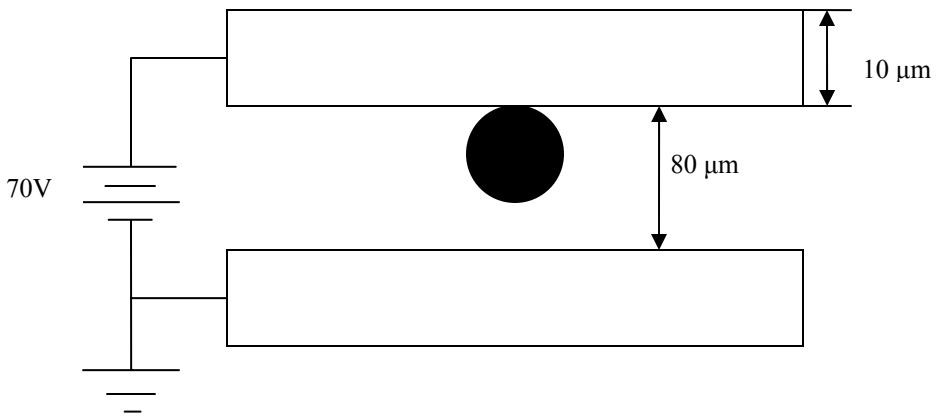

Figure 2-2: THz transmitter (F-Chip, GaAs10) with the 10 μm wide transmission lines separated by 80 μm and biased at 70 V.

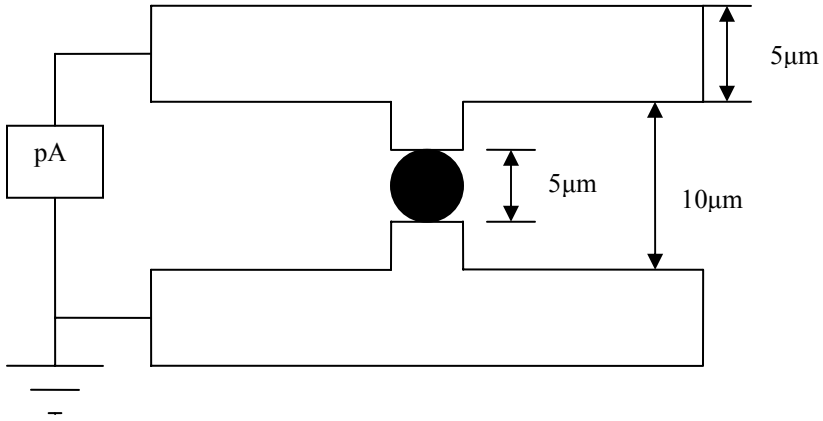

Figure 2-3: THz receiver (Max Chip, SOS Max 1) with 5 μm wide transmission lines connected to a current amplifier allowing a separation by 10 μm having the antenna dipole gap is also 5 μm.

2.2 Modified Focused beam THz-TDS system (8F confocal geometry)

The THz system used in this work is a photoconductive switch-based THz spectrometer having 4.5 THz (3 mm–67 μm) bandwidth as shown in Fig 2-4 [10, 13]. The system is aligned into an 8-F confocal geometry with four parabolic mirrors in order to achieve a 3.5 mm frequency-independent beam diameter, and for excellent beam-coupling between the transmitter and receiver [8, 9, 13]. An 800-nm, 25-fs optical pulse train generated from a self-mode-locked Ti:Sapphire laser is used to gate the photoconductive switches. The THz beam emitted from the GaAs transmitter is gathered by a silicon lens and then is collimated into a parallel beam by a parabolic mirror. To achieve a beam diameter comparable to the sample size an extra pair of parabolic mirrors of focal length 50.8 mm is placed midway in the THz beam path. The re-collimated beam is thereafter tightly focused onto another silicon lens at the SOS receiver. In this system a frequency dependent beam waist of 3.5 mm is obtained at midway of the two mirrors M_2 and M_3 [10,13].

Figure 2-5 shows the standard reference THz pulse and its corresponding amplitude spectrum of the 8-F THz-TDS system [12]. The measured pulse and their corresponding spectrum for this work has been described along with the analysis results of each samples in the following sections and shown in figures 5-2 and 5-7.

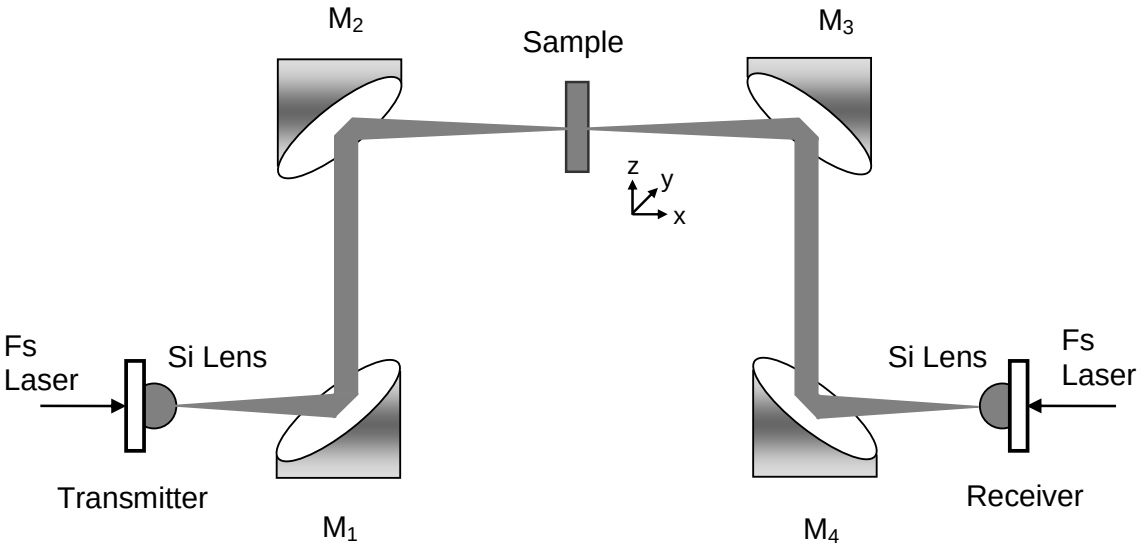

Figure 2-4: Modified THz-TDS setup using an 8-F confocal geometry. The sample to be characterized is placed at the 3.5-mm minimum waist position (center between M_2 and M_3). Focal Lengths of M_1 and M_4 are 101.6 mm while that of M_2 and M_3 are 50.8 mm.

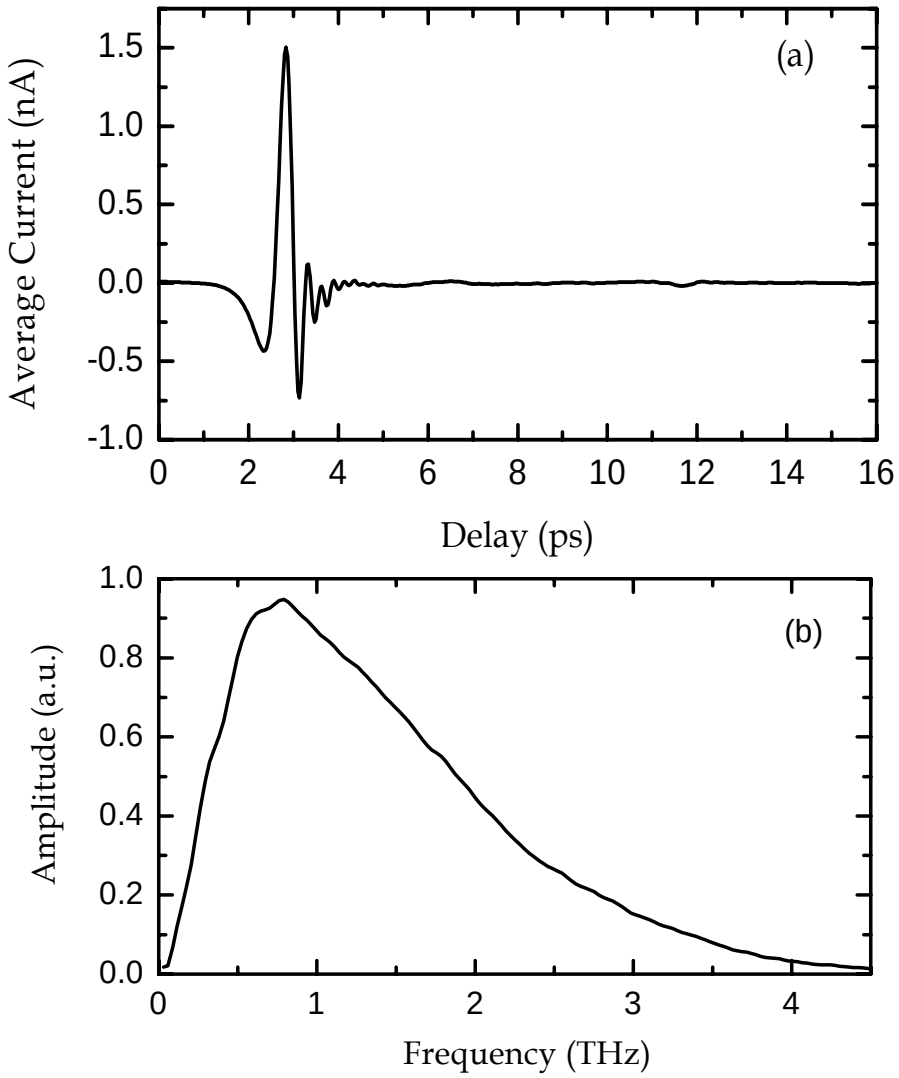

Figure 2-5 (a) Standard reference terahertz pulse propagating through air. (b) The corresponding amplitude spectrum of the reference pulse.

2.3 Determination of beam waist

In our experiment, the sample is located exactly at the center between the mirrors, M_2 and M_3 (at the beam waist) and care is taken so that the exposed area of the sample has almost the same dimension as that of the beam waist diameter. This is to make maximum utilization of the beam power and hence minimize loss. Hence, calculation of the beam waist of our system becomes utmost important.

Our system is a confocal system and all parabolic mirrors are treated as lens for the simplification in calculations. From the known values of the focal lengths obtained from the manual, we can easily calculate the distances between the mirrors, the distances between the mirror and the transmitter and the mirror and the receiver. The beam was also approximated to be a perfect Gaussian beam [12].

We assumed the initial waist of the beam to be 3.3 mm and then used simulation tool to obtain the beam waist profile (shown in Fig 2.6) and hence determined the actual beam waist diameter [12]. For using the simulation tool we needed to calculate the distance between each mirrors and between the mirrors M_1 from the transmitter silicon lens and between M_4 and receiver silicon lens. Hence the system manual was looked upon to obtain the focal lengths of each mirror.

We found that d_0 (distance between transmitter lens and mirror M_1) = f_1=101.6 mm, d_1 (distance between mirror M_1 and mirror M_2) =f_1+f_2=152.4 mm, d_2 (distance between

mirror M_2 and mirror M_3) $= 2f_2 = 101.6$ mm , d_3 (distance between mirror M_3 and mirror M_4) $= f_1 + f_2 = 152.4$ mm and d_4 (distance between mirror M_4 and receiver lens) $= f_1 = 101.6$ mm. Our calculated beam waist diameter was 3.5 mm. We observed from the beam waist profile curve that the beam waist was located exactly between the mirrors M_2 and M_3 hence the best place for samples.

2.4 Frequency Relation of the THz beam

In an 8-confocal system, the dependence of THz beam waist on frequency varies alternately. From the beam profile figure (Fig 2-6), we can see that at the silicon lens from where the beam emerges at the transmitter end, the beam waist is frequency dependent [12]. Then at the parabolic mirrors M_1 and M_2 there is a spread of the beam size, which increases with lower frequency. A frequency-independent focal spot is achieved midway between mirrors, M_2 and M_3 where the samples are located for THz-TDS characterization. When the THz beam propagates further from the focal spot on the way to the receiver side, we observe a nearly symmetric evolution of the beam waist. It becomes frequency independent at the silicon lens attached to the receiver. Hence, we have seen an alternating relation of THz beam waist on the 8-F geometry of the THz–TDS system used for the characterization of ZnO nanostructures.

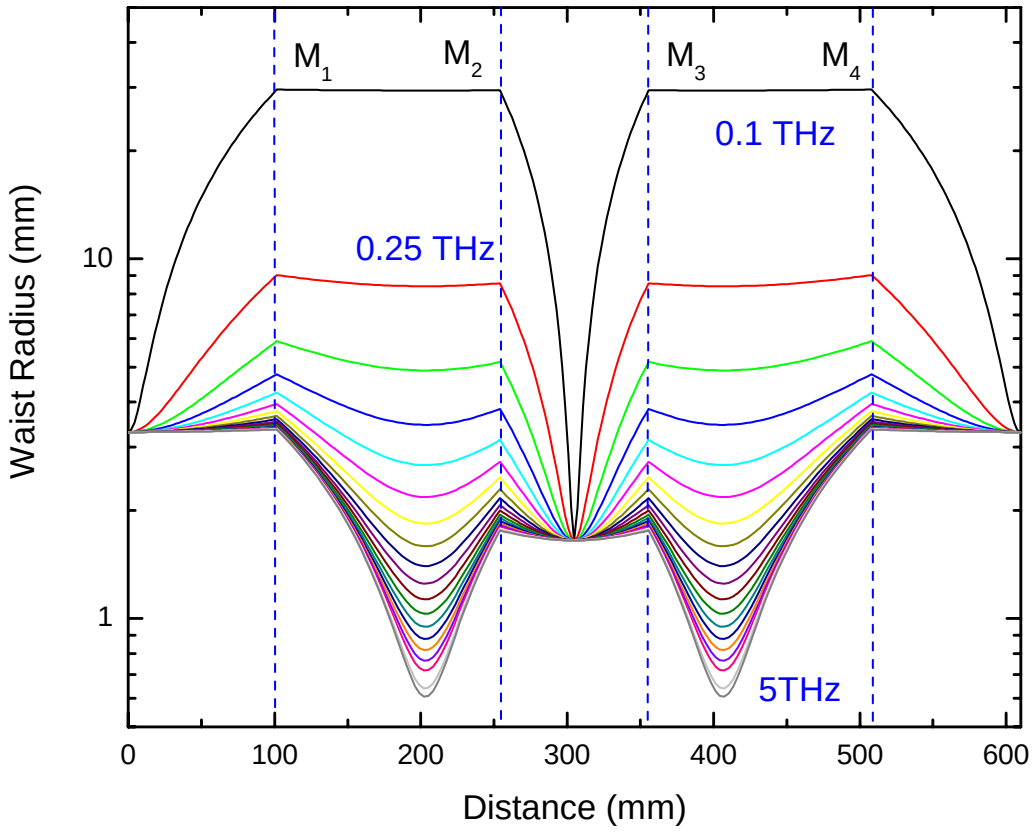

Figure 2-6: Calculated Gaussian beam profile shows the waist calculated for the 8-F confocal configuration.

2.5 Basic Cell Structures

The power absorption, refractive index and dielectric constants of the samples are measured on the 8-F confocal geometry as described above. The reflection of the THz beam on the front and the back side of the cell is taken into consideration. A distinct separation between the transmitted pulse and the first reflected pulse always enables the data analysis only on the first transmitted pulse while ensures sufficient characterization accuracy. The schematic diagrams of the cross-sectional areas of the cells (*both reference and sample*) are shown in figure 2-7. The cells were made of a 640-μm-thick, p-type silicon wafer having a resistivity of ρ = 20 Ω-cm.

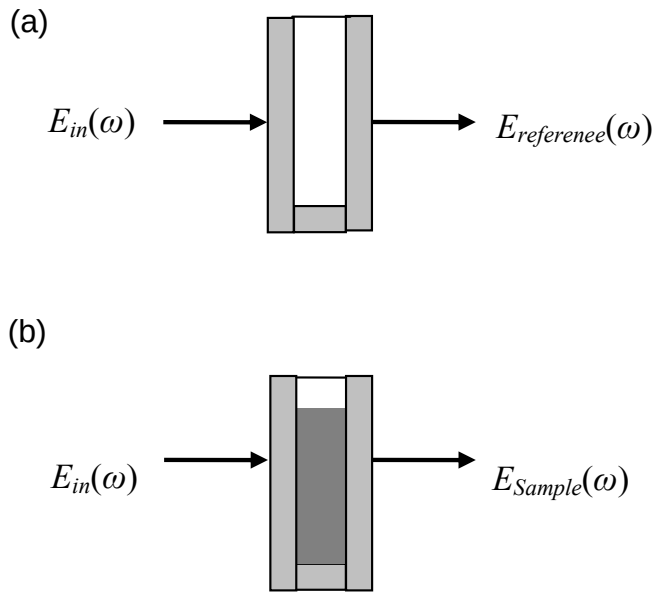

Figure 2-7 Diagrams of the cross-sectional areas of (a) Empty reference cell (b) Cells holding the samples.

CHAPTER III

Data Extrapolation

3.1 Basic Data analysis

The sample under inspection is placed at the tightly focused beam waist position. We have seen that it is this particular point where the beam is most tightly focused and the beam size is frequency independent [10]. We will assume that the amplitude of the THz beam without and with sample in the cell are referred as $E_{reference}(t)$ and $E_{sample}(t)$, respectively

Below are the transmission equations for the cell arrangement (Fig 2-7) [10, 12, 15, and 17]:

$$E_{reference} = E_{in} t_{sa} t_{as} \exp\left(\frac{i2\pi nd}{\lambda}\right), \tag{3-1}$$

$$E_{sample} = E_{in} t_{sm} t_{ms} \exp\left(\frac{i2\pi nd}{\lambda}\right)\exp\left(\frac{-\alpha d}{2}\right) \tag{3-2}$$

In the above expression E_{in} is the amplitude of the input THz pulses and t_{sa} , $t_{as,}$ $t_{ms,}$ t_{sm}

are referred to as Fresnel's coefficients where '*a*' denotes air, '*s*' denotes substrate and '*m*' denotes material. Here α and n are power absorption and refractive index, respectively.

3.2 Calculation of Real and imaginary Dielectric Constants.

The frequency dependent effective complex dielectric response of a sample can be determined by the recorded data of power absorption and the refractive index through the relationship: $\varepsilon(\omega) = (n_r + in_i)^2$, and the imaginary part of the refractive index can be obtained by the relation: $n_i = \alpha\lambda / 4\pi$. From the above two expressions the real and imaginary components of the complex dielectric function can be obtained and can be written as follows [10, 17]:

$$\varepsilon_r = n_r^{\,2} - (\alpha\lambda_0 / 4\pi)^2, \tag{3-3}$$

and

$$\varepsilon_i = \alpha n_r \lambda_0 / 2\pi\,. \tag{3-4}$$

CHAPTER IV

RELATED THEORIES

4.1 Simple Effective Medium Theory (EMT)

Effective medium theory (EMT) has been a prevalent tool used to analyze the material's optical properties in the composite medium. By using this technique the properties are determined by the known property of its constituent [20]. Reflecting confinement effects of the crystalline structures are usually studied by the effective medium approach. The effective medium approach appears to be really effective for the closely packed structures. One of the simplest approaches of the effective medium theory was devised by using the Maxwell-Garnett (MG) model predicted in 1904 [21]. The MG model devised to characterize the dielectric properties of the multiphase mixture was developed using Clausius and Mosotti theory. The effective dielectric permeability according to the MG model was stated as [20, 21]:

$$\frac{\bar{\varepsilon}^{MG} - \varepsilon_m}{\bar{\varepsilon}^{MG} + 2\varepsilon_m} = f \frac{\varepsilon - \varepsilon_m}{\varepsilon + 2\varepsilon_m}, \tag{4-1}$$

where $\bar{\varepsilon}^{MG}$ is the effective dielectric permeability of the sample concerned (spherical particle was used in original case) and ε_m is the characterized surrounding medium. This

theory is made under the assumption that a sufficiently large separation between the particles existed for independent scattering to occur and for the Lorentz local-field correction to apply [20,21]. The simplicity of the MG model makes it a very popular and hence this model has been used over and over again for treating optical properties of various structures.

By using the celled approach and by using the simple mixing model it is possible to calculate the optical properties of the nano-crystals embedded in the host crystals, vacuum and in layered structures [20]. The constructed cell is the one that contains the objects or sample to be treated while the other cell is used as reference with respective amount of surrounding matrix or vacuum. The cell structures that are used in our case has been discussed in the section 2.4, and has been diagrammatically shown in Fig 2.7.

The concept of EMT lies with macroscopic objects where the sizes of the structures are treated with the cell calculations [20]. The properties, mainly their optical properties are not the simple properties of their respective bulk material, rather they are the effects which occur due to the confinement, more specifically due quantum confinement of the electronic states. As stated above that in the effective medium approach, the properties of the composite material are characterized and predicted with from its known constituent properties and hence the optical properties of the composite and host material has to be known. So, the optical properties can be extracted and predict the composite properties by applying the effective medium theory [20].

Basically two steps are used to extrapolate the composite-material properties by using EMT. First the material dielectric function $\varepsilon_m(\omega)$ of nanostructure of certain radius is extracted from the dielectric function $\varepsilon(\omega)$ derived from composite material using the known dielectric function, ε_h of the host material. For comparison, a simple mixing model is then used which can be written as follows:

$$\varepsilon(\omega) = f\varepsilon_c(\omega) + (1-f)\varepsilon_h(\omega), \tag{4-2}$$

where, f is the filling factor given by ratio of the crystalline volume and the total cell volume. It is to be noted here that while Maxwell-Garnett (MG) model explain about isotropic condition, the Bruggemann model takes into account the correlations due to the self-consistent determination of the dielectric properties [20].

In the effective medium mixing model, the dielectric function is only valid in terms of embedment with different filling factors which implies to similar environment to that of the original one. The description of the quantum size effect is therefore a close generalization of the original concept of the effective medium approach. Now the applicability of effective medium mixing model is much limited to the energies below the main peak of absorption. A modification in the EMT, which will be not accounted here will take into consideration of other absorption peaks [20]. The application and the effectiveness of the effective medium approach described above depend much on the energy and the size rage of the particle concerned.

Limitations of simple Effective Medium Theory (EMT):

In order to extract the dielectric function $\varepsilon_m(\omega)$, pertaining to the nanostructures, a simple mixing model is being used which is stated as:

$$\varepsilon_{eff}(\omega) = f\varepsilon_m(\omega) + (1-f)\varepsilon_h = \varepsilon_{effr}(\omega) + i\varepsilon_{effi}(\omega),$$

where, f is the filling factor determined by the volume ratio. There can be certain limitations in using this model. The quantity $\varepsilon_m(\omega)$ represents the optical properties of an effective material which rather reflects the quantum size effects, characterized by size of the sample. Hence, $\varepsilon_m(\omega)$ obtains it substantial meaning only with respect to embedding in surrounding materials. This independent–particle expression of dielectric function will be exact if the wave functions of the electrons of the structures and the host material are strongly localized. In order to characterize more densely packed samples and for higher value of filling factor, more complex models like Maxwell-Garnett theory or Bruggeman's theory can be implemented.

4.2 Pseudo-Harmonic Approximation

The ionic crystal's optical absorptions are attributed by the lattice-vibrations in the far-terahertz regime. An interaction between the radiation field with the fundamental lattice vibration results in the absorption of the electromagnetic wave owing to the creation or the annihilation of lattice vibration. Hence in the frame of the classical theory of independent pseudo-harmonic approximation, contribution of phonons are considered in the dielectric function [17]:

$$\varepsilon(\omega) = \varepsilon_\infty + \frac{(\varepsilon_0 - \varepsilon_\infty)\omega_{TO}^2}{\omega_{TO}^2 - \omega^2 - i\Gamma\omega}, \tag{4-3}$$

where, $\varepsilon_{st} = (\varepsilon_0 - \varepsilon_\infty)$, ε_∞ is the high-frequency dielectric constant, ε_0 is the low-frequency dielectric constant, ω_{TO} is the frequency of the TO phonon mode where as Γ is considered here to damping considered here to be the damping constant.

By using equation 4.12 and equation 4.3, we obtain the real and imaginary parts as:

$$\varepsilon_r(\omega) = \varepsilon_\infty + \frac{(\varepsilon_0 - \varepsilon_\infty)\omega\Gamma\omega_{TO}^2}{(\omega_{TO}^2 - \omega^2)^2 + \Gamma^2\omega^2}, \tag{4-4}$$

$$\varepsilon_i(\omega) = \frac{(\varepsilon_0 - \varepsilon_\infty)\omega\Gamma\omega_{TO}^2}{(\omega_{TO}^2 - \omega^2)^2 + \Gamma^2\omega^2} \tag{4-5}$$

The calculations and exact steps to obtain the real and imaginary parts relations of equation 4.4 and 4.5 is shown in *Appendix A*. These real and imaginary dielectric constants are used to obtain the effective real and imaginary dielectric constants, $\varepsilon_{eff}(r)$ and $\varepsilon_{eff}(i)$, which are used to fit the corresponding experimentally obtained values. The calculation to obtain the effective real and imaginary dielectric constants is shown in *Appendix B*.

These effective real and imaginary dielectric ($\varepsilon_{eff}(r)$ and $\varepsilon_{eff}(i)$) constants are again used to obtain the theoretical values of the real refractive index (n_r) and the power absorption

coefficient (α) which are again fitted with their corresponding experimental results. The calculation to obtain n_r and α are shown in *Appendix C.*

4.3 Procedure Followed

The complex dielectric responses of the ZnO nanostructure can be achieved by the power absorption relation, $\varepsilon(\omega) = (n_r + in_i)$ while the imaginary part n_i is corresponds to the power absorption as $n_i = \alpha\lambda / 4\pi$.

Semiconductor crystals have the optical vibrations which are attributed by the lattice vibrations. The classical theory of independent pseudo-harmonic model explains the dielectric response in accordance to the Lorentz dispersion theory in conjunction with that of the Huang equations. The dielectric function is related as [16]

$$\varepsilon(\omega) = \varepsilon_\infty + \frac{(\varepsilon_0 - \varepsilon_\infty)\omega_{TO}^2}{\omega_{TO}^2 - \omega^2 - i\Gamma\omega}, \tag{4-6}$$

where ε_∞ is the high frequency dielectric constant, ε_0 is the low-frequency dielectric constant, Γ is the damping constant whereas ω_{TO} the optical transverse mode. The complex frequency dependent dielectric constant as described in equation (4.1) can be

written as a set of two separate variables which are the real and the imaginary parts. Hence, $\varepsilon(\omega)$ can be written as:

$$\varepsilon(\omega) = \varepsilon_r(\omega) + i\varepsilon_i(\omega) \tag{4-7}$$

with ,

$$\varepsilon_r(\omega) = \varepsilon_\infty + \frac{\varepsilon_{st}\left(\omega_{TO}^2 - \omega^2\right)\omega_{TO}^2}{\left(\omega_{TO}^2 - \omega^2\right)^2 + \Gamma^2\omega^2}\ , \tag{4-8}$$

$$\varepsilon_i(\omega) = \frac{\varepsilon_{st}\omega\Gamma\omega_{TO}^2}{\left(\omega_{TO}^2 - \omega^2\right)^2 + \Gamma^2\omega^2}\ . \tag{4-9}$$

And the effective dielectric function, ε_{eff} of the ZnO tetrapods can be found by the equation:

$$\varepsilon_{eff}(\omega) = f\varepsilon_m(\omega) + (1-f)\varepsilon_h = \varepsilon_{effr} + i\varepsilon_{effi}\,, \tag{4-10}$$

where $\varepsilon_{eff}(\omega)$ is the effective complex dielectric constant whereas ε_m and ε_h are the dielectric constant of the sample and host which air in our case and hence equals unity. In the above simple EMT f is given by the fractional volume of the particle that is the ratio of the density calculated from the measured mass and volume of the particle to the actual density of the particle $(5.7 gm/cm^{-1})$ in this case. The ε_m term presented in the above EMT equation is estimated by a pseudo-harmonic equation described within the frame of classical theory which is given by the following equation [16, 17, 18]:

$$\varepsilon(\omega) = \varepsilon_{\infty} + \frac{\varepsilon_{st}\omega_{TO}^2}{\omega_{TO}{}^2 - \omega^2 - i\Gamma\omega}, \tag{4-11}$$

where ε_{st} is the oscillator strength, ε_{∞} is the high frequency dielectric constant and ω_{TO} is the frequency of the transverse optical mode and Γ being the damping constant. Again we can split the complex dielectric constant of the sample into its corresponding real and imaginary parts, described as:

$$\varepsilon_m(\omega) = \varepsilon_{rm}(\omega) + i\varepsilon_{im}(\omega). \tag{4-12}$$

Again from equation (4.6) we can calculate effective real dielectric constant and effective imaginary dielectric constant from the known calculated values of ε_{rm} and ε_{im} as :

$$\varepsilon_{eff}(r) = f\varepsilon_{rm}(\omega) + (1 - f) \tag{4-13}$$

and

$$\varepsilon_{eff}(i) = f\varepsilon_{im}(\omega) \tag{4-14}$$

A good match between the experimental data and the fitting indicate the presence a dominant TO-mode centered at a frequency of $\omega_{TO}/2\pi$ with a line-width $\gamma/2\pi$ and a strength ε_{st} given by the adding ε_0 and ε_{∞}.

CHAPTER V

Experiments and Results

5.1 ZnO tetrapods

Our first sample analyzed is ZnO tetrapod. The power absorption, refractive index, and the complex dielectric function were measured in the frequency range from 0.2 to 3.5 THz. Further, a simple effective medium theory was employed to study the low-frequency dielectric properties of ZnO tetrapods [19]. In course of analysis, an association with the transverse optical E_1 phonon mode was found, which corresponds well to that of the bulk ZnO.

5.2 Sample description

Zinc oxide (ZnO) is an excellent II-VI compound semiconductor for low-voltage and short-wavelength optoelectronics applications owing to its direct wide band gap of 3.37 eV, high exciton gain, and a large exciton binding energy of ~60 meV with minimum fabrication barrier, rather high mobility (200 cm^2/Vs) and high resistivity making the single-crystal ZnO an ideal choice for high power THz generation [1-3,5]. Detail study of the properties of ZnO tetrapods is essential to understand the physics of low-dimensional system and their possible potential applications such as laser and hardening [2]. The resent interest on the tetrapod structures of ZnO have been mainly due to its intriguing

lasing properties [23,24]. The tetrapod structure of the ZnO can be a good choice of being a detector because its gas sensing properties specially with methane and methanol at various temperatures [25]. Again the ZnO tetrapods are expected to exhibit some special properties because of their single crystalline structure and because of its controllable morphology [26]. When ZnO tetrapods were doped with Mn, the structures were found to be ferromagnetic with Curie temperature ~50 K. Analysis of these doped structures showed a large coercive field, which enabled and opened the gateway for the electromagnetic and spintronics applications leading method to combine microelectronics and nanoelectronics with spin-dependent effects for the next generation devices [27]. Recent findings show that ZnO tetrapods have shown intriguing lasing properties by making the arm lengths very compatible to the excitation wavelength [23,24].

The vapor phase transport method was used to grow the ZnO tetrapods were by heating the Zn powder to 700 ºC in a quartz tube furnace at ambient pressure and with the flow of argon gas [24]. By sonicating in methanol the individual tetrapod samples were isolated. Shape and size of the ZnO tetrapods were found by inspecting under scanning electron microscope and optical microscope, while X-ray diffraction revealed hexagonal wurtzite structures. The diameters of the legs were estimated to be 200 and 800 nm while the length of the legs were between 10-30 μm [27, 28]. The SEM images of a bundle of ZnO tetrapods are shown below in Fig. 5.1.

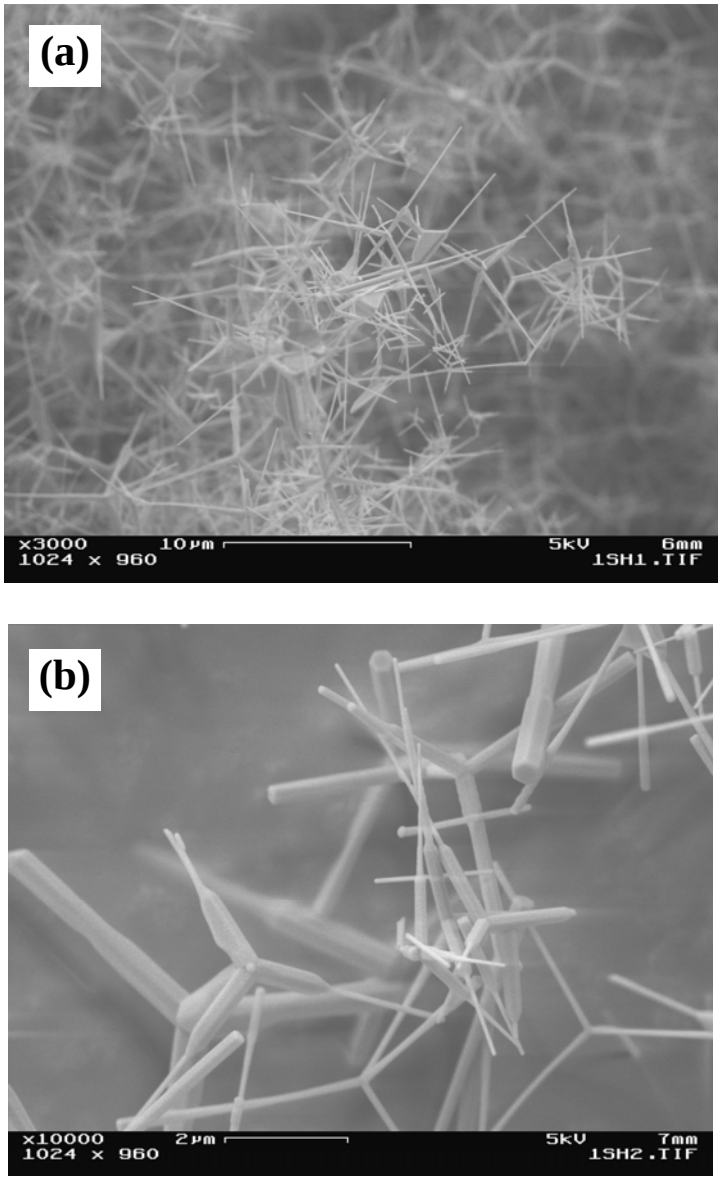

FIG. 5.1 The SEM images of ZnO tetrapod bundle with leg diameter of 200- 800 nm and length of 10 -30 μm.

5.3 Analysis Procedure for ZnO tetrapods

The ZnO tetrapod samples for analysis were placed in a cell, made from carefully diced p-type silicon wafer of 640 μm thickness having a resisivity (ρ = 20 Ωcm), with dimensions of 10.9 mm × 11.0 mm [19]. A spacer made from the same material with a thickness of 1.288 mm was introduced between the cell windows. An identical empty cell was used as a reference. Both cells were placed in an aluminum holder and centered over a 5-mm-diameter hole, which defines the optical aperture. The structure of the cell has been discussed in section 2.4 and shown in Fig 2.7. The aluminum holder unit was placed exactly at the beam waist of the THz-TDS system as shown in Fig 2.4. The THz-TDS system used for this work is described in section 2.1 and 2.2.

5.4 Results and discussion for ZnO tetrapods

The dielectric and optical properties of ZnO tetrapods are extrapolated using a simple effective medium theory [8, 20]. The transmitted THz pulses through both the reference and ZnO samples are shown below in Fig 5.2(a). Compared to the reference, the signal obtained from ZnO tetrapods has a time delay, as well as reduced amplitude due to absorption. A relatively clean separation in time between the main transmitted pulse and the first refection allows us to perform the data analysis on the main pulse only [10]. The sample and the reference pulses were then Fourier transformed to achieve the corresponding complex amplitude spectra which are shown below in Fig. 5.2(b).

The power absorption and refractive index were extrapolated. The ratio between the amplitude spectra of the reference and that of the sample gave the effective absorption by the sample whereas the phase shift was calculated to determine the refractive index [30]. The frequency-dependent power absorption coefficient $\alpha(\omega)$ and the refractive index $n(\omega)$ are plotted as open circles in Fig. 5.3. The measured power absorption increases as a function of frequency and no prominent absorption peak is observed below 3.5 THz, whereas the refractive index approaches a constant 1.041. The frequency-dependent dielectric response $\varepsilon(\omega)$ is described by the relationship, $\varepsilon(\omega) = \varepsilon_r(\omega) + i\varepsilon_i(\omega) = [n(\omega) + ik(\omega)]^2$, where the imaginary part of the refractive index k is related to the power absorption as $k(\omega) = \alpha(\omega)\lambda_0 / 4\pi$, $\varepsilon_r(\omega)$ and $\varepsilon_i(\omega)$ are the real and imaginary part of the dielectric function [10]. Since the ZnO tetrapods are loosely packed, the EMT is employed to obtain the true dielectric function of ZnO tetrapod [8, 20], $\varepsilon_{eff}(\omega) = f\varepsilon_m(\omega) + (1-f)\varepsilon_h$, where the filling factor f defines the volume fraction of the tetrapods and was measured during the experiment. The effective medium theory used here is described in more details in section 4.7. ε_h and ε_m are the dielectric constants of host medium and pure ZnO tetrapods, respectively.

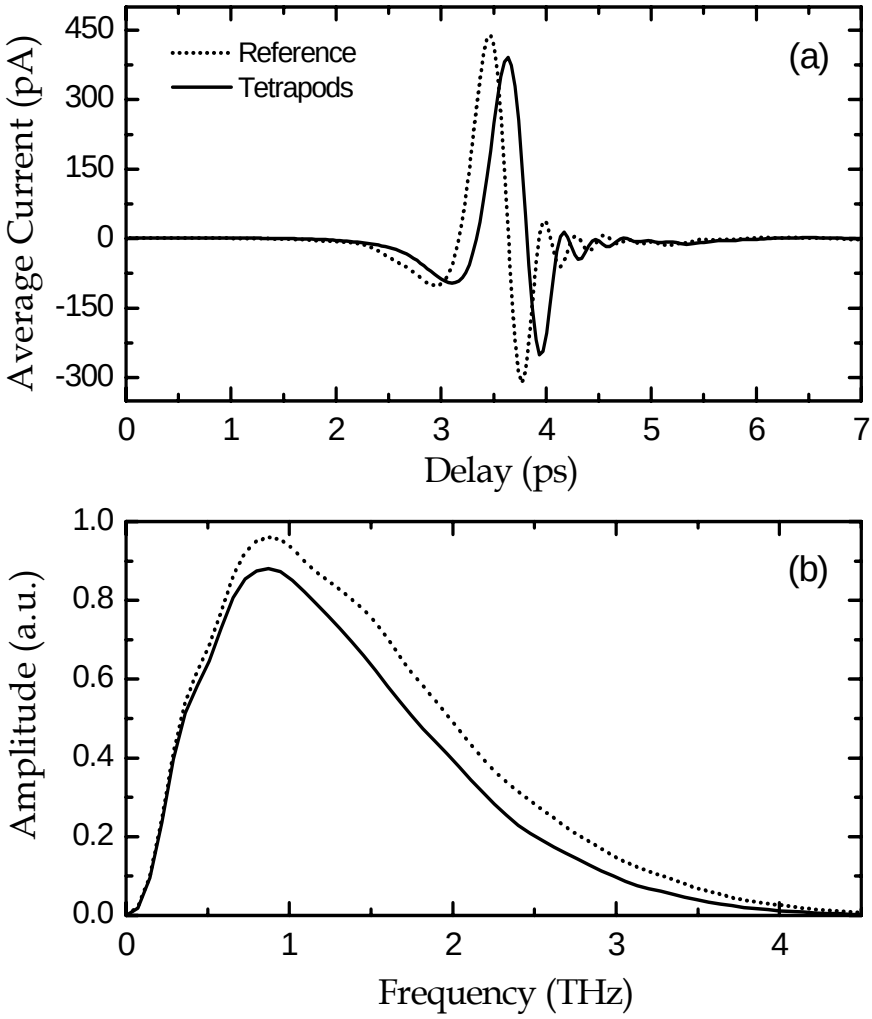

FIG. 5.2 (a) Measured reference and sample pulses, and (b) the corresponding Fourier-transformed spectra (Solid lines represent the sample curves while the dashed lines represent the reference curves).

In our case, $\varepsilon_h = \varepsilon_{air} = 1.0$, and the frequency-dependent dielectric function of the pure tetrapods $\varepsilon_m(\omega)$ can be represented by the equation below:

$$\varepsilon_m(\omega) = \varepsilon_\infty - \frac{\omega_p^2}{\omega^2 + i\gamma\omega} + \sum_j \frac{\varepsilon_{st_j}\omega_{TO_j}^2}{\omega_{TO_j}^2 - \omega^2 - i\Gamma_j\omega}, \tag{5-1}$$

where ε_∞ is the high-frequency dielectric constant, the second term describes the contribution of free electrons or plasmons, and the third term is due to the contribution of optical phonons. The key parameters describing the dynamics of free electrons or plasmons in a semiconductor are the plasma frequency $\omega_p = \left(Ne^2/\varepsilon_0 m^*\right)^{1/2}$ and the carrier damping constant γ, where N is the carrier density, m^* is the effective mass of the electron, and ε_0 is the free-space permittivity 8.854×10^{12} F/m. The mobility can be obtained from $\mu = e/(m^*\gamma)$. The summation term in Eq. (4.6) is over all lattice oscillations with the *j*th transverse optical (TO) frequency $\omega_{TO\,j}$, oscillator strength $\varepsilon_{st\,j}$ and phonon damping constant Γ_j. For the hexagonal wurtzite bulk ZnO in the THz region, it is known that the main dielectric response is from the E_1(TO) vibrational mode [19,31]. Thus, based on Eq. (4.6), the dielectric function $\varepsilon(\omega)$ describing our measured sample can be simplified as shown in below and described in equation 4.3

$$\varepsilon_m(\omega) = \varepsilon_\infty + \frac{\varepsilon_{st}\omega_{TO}^2}{\omega_{TO}^2 - \omega^2 - i\Gamma\omega} \tag{5-2}$$

The real and imaginary dielectric constants are more in Fig 5.4 below and are represented by open circles.

The simple effective medium theory in tandem with the classical theory of independent pseudo-harmonic approximation allows us to obtain a theoretical fit for the calculated refractive index and the power absorption. The procedure followed to calculate the theoretical value of the refractive index and power absorption is described in section 4.1 and *Appendix C*. The refractive index and the power absorption fitting with solid lines is shown below in Fig 5.3. Based on Eq. (4.7), the solid curves in Fig.5.3 presents a good fit on the experimental data (solid circles) of single crystalline ZnO using the parameters: $\varepsilon_{\infty} = 1.5$, $\varepsilon_{st} =$ 3.40, $\omega_{TO}/2\pi =$ 12.41 ± 0.2 THz and $\Gamma/2\pi = 21.0 \pm 0.2$ THz.

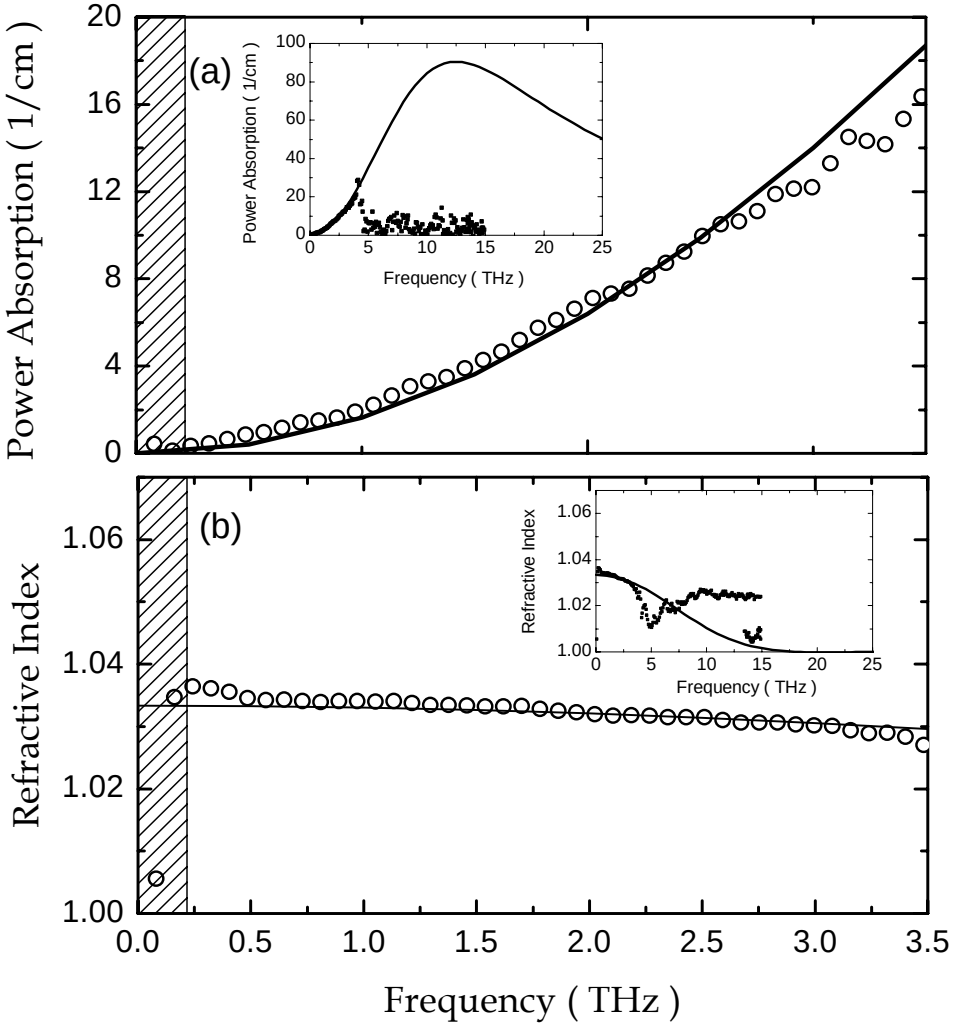

FIG. 5.3 Comparison of measured results (open circles) with theoretical fitting (solid lines) for ZnO tetrapod structures: (a) power absorption $\alpha(\omega)$; (b) refractive index $n(\omega)$. (Inset shows the same curves up to 25 THz).

The real and imaginary dielectric constants are more in Fig. 5.4 below and are represented by open circles. Again, by combining equation 4.3 and the effective medium theory equation we obtain a theoretical fit for the experimentally obtained real and imaginary dielectric constants by using the same parameters used to obtain the theoretical filling for the refractive index and power absorption. In figure 5.4, the solid lines represents the theoretical fit for the experimentally obtained dielectric values. The value of the filling factor f used to fit all the refractive index, absorption, and complex dielectric is 0.0173649. The fitting reveals the presence of a dominant TO-phonon resonance of ZnO tetrapods, centered at $\omega_{TO}/2\pi$=12.41 THz with a phonon damping constant $\Gamma/2\pi$ = 21.0 THz and a strength ε_{st}= 3.40. It is worth noting that such a TO mode at 12.41 THz is a typical transverse optical mode in the bulk ZnO of wurtzite structure with the assignment E_1(TO) [19,31]. Let us assume that τ is the TO phonon lifetime, such that we have $\tau = 1/\Gamma$ with value $\tau/2\pi$ = 47.6 fs. In fact, τ depends very minutely on the type of scattering mechanism and a number of different scattering laws usually define the various lifetimes. Here, the obtained TO phonon lifetime τ results and depends mainly upon calculation of absorption in which scattering from transverse optical phonon has been considered [32].

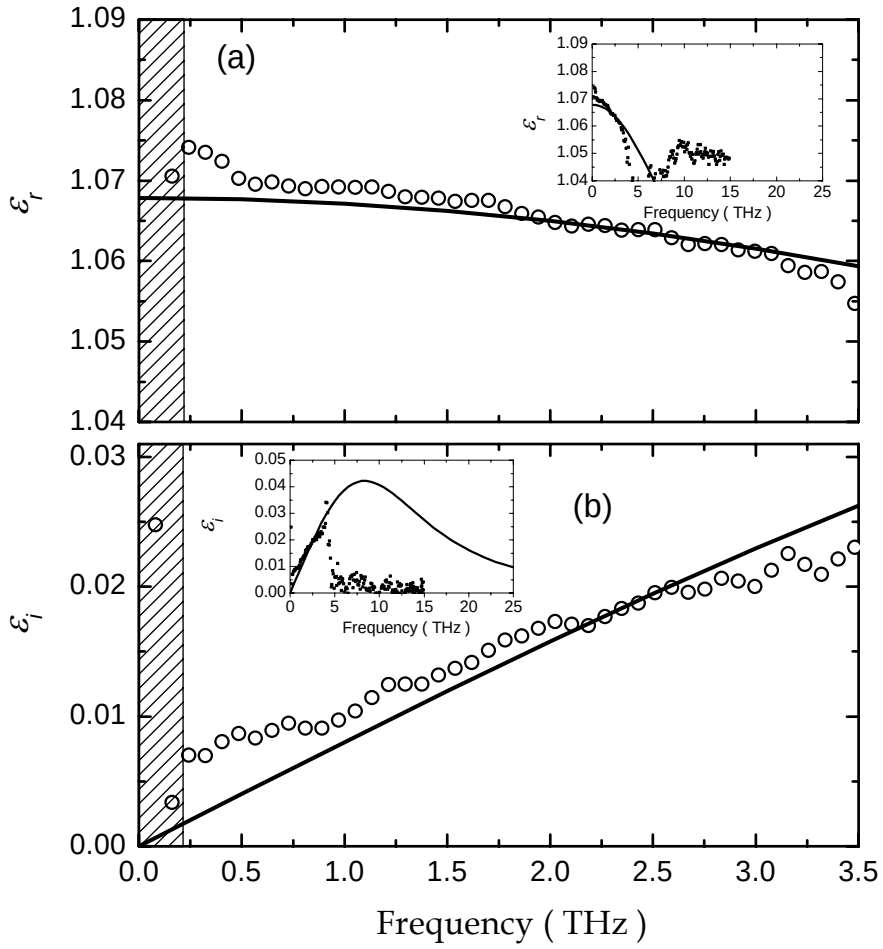

FIG. 5.4 Frequency-dependent complex dielectric function of ZnO tetrapod structures: (a) real part $\varepsilon_r(\omega)$, and (b) imaginary part $\varepsilon_i(\omega)$. The solid curves and the open circles represent the theoretical fitting and the experimental data, respectively. (Inset shows the same curves up to 25 THz).

In order to have a clearer understanding of the results of the analysis obtained in the THz regime, the THz-TDS results of the single crystal of ZnO is obtained and compared. Figure 5.4 shows the comparison between the power absorption and refractive index of ZnO with that of the single crystalline ZnO. The single crystal ZnO sample is of high purity (>99.99%) which is also undoped. The dimensions of this sample used were 5 mm × 5 mm × 0.5-mm-thick, free standing single crystal having wurtzite structure. Hence, it is evident from Fig. 5.4, that the THz spectra of single-crystal ZnO shows similar behaviors as that of ZnO tetrapod structures but with a lager index of refraction, 2.80, than the value of ZnO tetrapod, 1.03. Similar methods as that of ZnO tetrapods were used to calculate the theoretical fit for the single crystal structure. Based on Eq. (4.3) and the effective medium theory , discussed previously, the solid curves obtained and shown in Fig. 5.4 presents a good fit on the experimental data (solid circles) of single crystalline ZnO using the parameters: $\varepsilon_{\infty} = 3.705$, $\varepsilon_{st} =$ 4.065, $\omega_{TO}/2\pi = 12.42$ THz and $\Gamma/2\pi$ =0.82 THz. It demonstrates that the THz spectra of single crystal ZnO are also dominated by the E_1(TO) phonon mode centered at the frequency 12.42 THz. All of these features clearly imply that ZnO tetrapod structures represent quite similar characteristics as the single-crystal ZnO in the low-frequency THz regime.

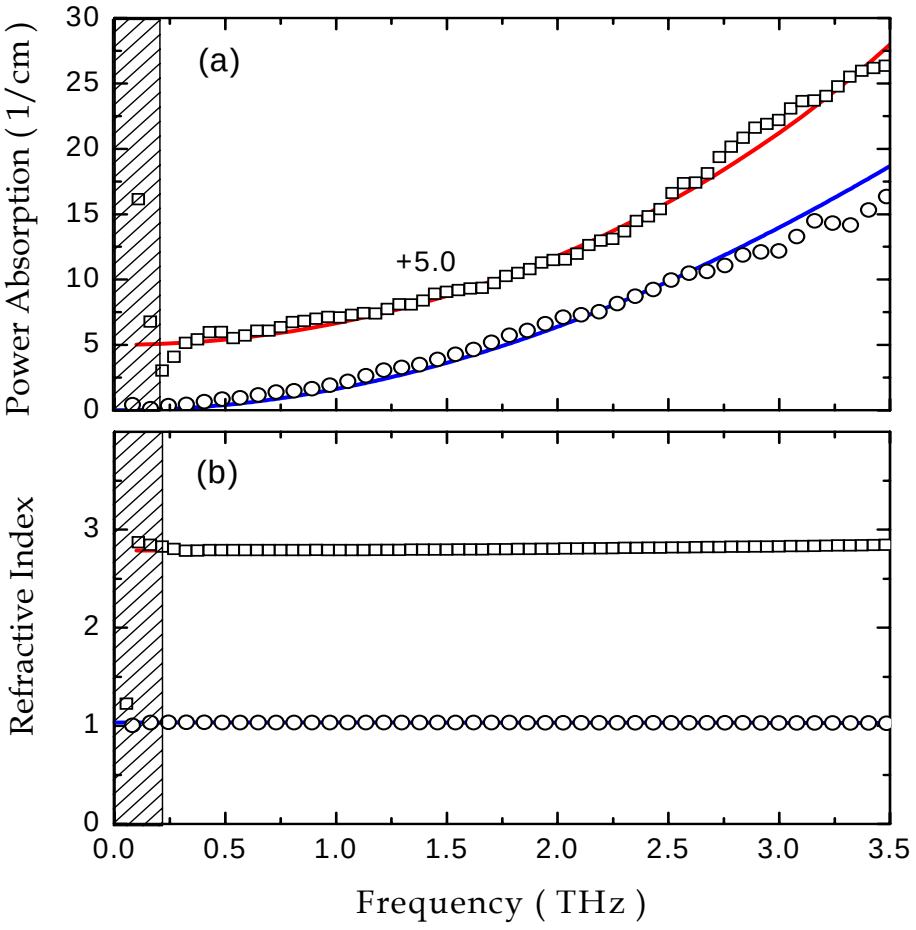

FIG. 5.5 (Color online) Comparison of (a) measured power absorption (offset by 5.0 1/cm) and (b) refractive index of ZnO tetrapods (open circles) with that of single-crystal ZnO (solid circles). The solid curves are the corresponding theoretical fit.

Usually it is observed that the nanostructures show quite a bit of dissimilar properties as compared to its bulk structure. But here we obtained and observed from the THz-TDS that the nanostructure and the bulk structure has very similar THz spectra with apparently no differences. It indicates that the ZnO tetrapods keep almost overall crystal structure of the bulk ZnO. This result is also quite consistent with that of ZnO nanoparticles or ZnO nanotubes [33, 34].

When the radius of the nanostructures tends to approach the Bohr radius of the exciton, the quantum confinement effect will become predominant and noticeble. The diameter of the legs in ZnO tetrapods is between 200 and 800 nm which are much larger than that of the Bohr radius of ZnO (the calculated value is about 2 nm). This is why there are no obvious distinctions observed in dielectric properties between the single-crystal ZnO and tetrapod structures [34].

5.5 ZnO nanowires

The next sample analyzed is another ZnO crystalline structure, the nanowire. The optical and dielectric properties, in the range of 0.1 to 4.5 THz using THz time-domain spectroscopy (THz-TDS) are being characterized.

5.6 Description of ZnO nanowires

Figure 5.5 shows the images of the ZnO samples. The ZnO nanowire used in our case has been produced, using a microemulsion-mediated hydrothermal process under very mild conditions [35]. This process is very simple and direct unlike complex and expensive vapor transport and physical vapor deposition processes having rigorous experimental conditions [35].

In this process the nanowire was prepared by quaternary microemulsion by mixing 1 gram of cetyltrimethylammoniumbromide (CTAB, AR) and 1.2 mL of $Zn(OH)_4^{-2}$. While making this solution the pH value of the mixture of zinc acetate and NaOH was adjusted to 14. 3 mL of *n*-hexanol and 10.2 mL of *n*-heptane was used as the reaction media. Care was taken such that, there was a constant stirring and thereafter the mixture was transported into a 25 mL teflon-lined autoclave which was heated to 140° C for about 13 hours. A white precipitate was formed which was then washed several times using ethanol and diluted water. And, lastly nanowires of ZnO was obtained by centrifugation and drying in vacuum at 60-70° C [35].

The morphology of the ZnO thus prepared was examined very carefully by the scanning electron microscope (SEM, Amary, FE-1910) and transmission electron microscope (TEM, Hitachi , H-9000NAR). Figure 5.6(a) and 5.6(b) shows typical SEM and TEM images respectively. The SEM picture reveals that the nanowires of ZnO has the typical diameter of 30-150 nm with aspect ratio larger than 50. The TEM image of the same shows a diameter of 30 nm with a length of up to 3 μm [35].

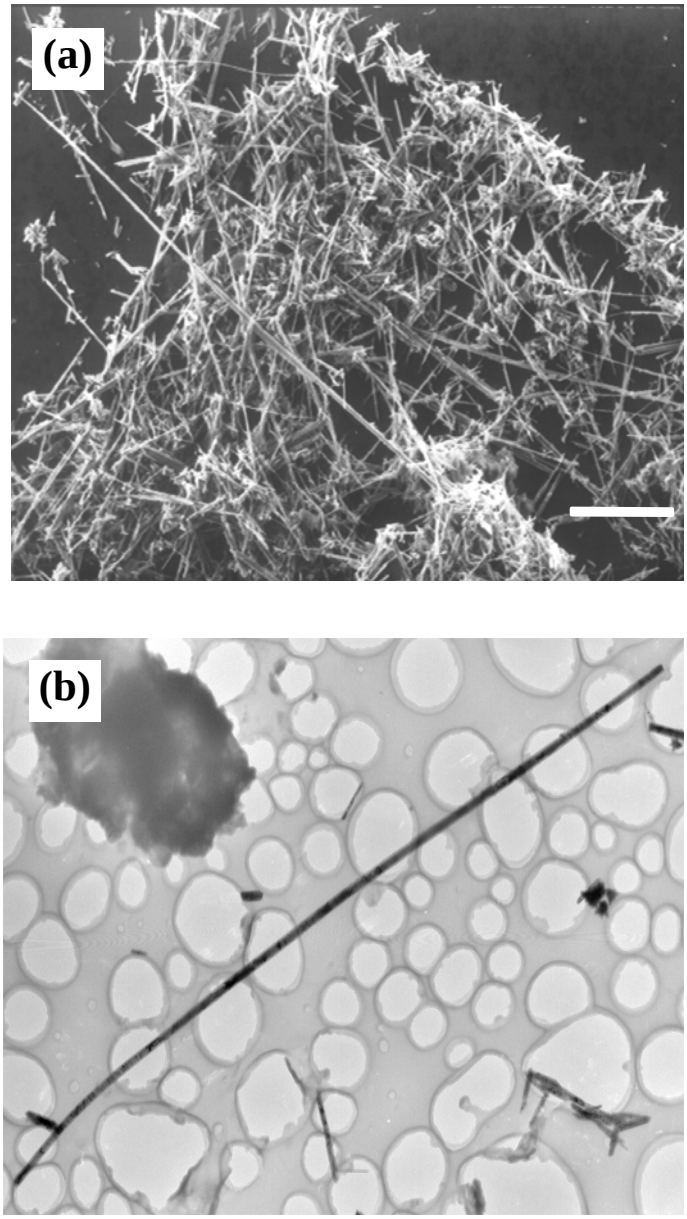

Figure 5.6 SEM image (a) and TEM image (b) images of ZnO nanowires

5.7 Analysis Procedure of ZnO nanowires

These as-obtained sample of ZnO nanowires were then placed in the cells by the application of neutral pressure. The structures of the reference and sample cells are shown in Fig. 2.7. The dimension of the cell holding the ZnO nanowires is 6 mm × 12 mm × 0.628 mm. Both cells were placed in an aluminum holder and centered over a 5-mm-diameter hole, which defines the optical aperture. The aluminum holder unit was placed exactly at the beam waist of the THz-TDS system as shown in Fig 2.4. The THz-TDS system used for this work is described in section 2.1 and 2.2. Amplitude transfer function for parallel dielectric slab is being used for data extrapolation [10]. Due to relatively clean separation in time between the main transmitted pulse and the first reflection, the data analysis was performed on the main pulse only [9]. This approximation makes the first transmitted pulse free of oscillation enabling us to calculate the power absorption α and refractive index n rather very precisely [9].

5.8 Results obtained and discussion for ZnO nanowires

Figure 5.6(a) shows the measured reference and sample THz pulse obtained from the 8-F confocal system (described in the section 2.1 and 2.2) used for the analysis of the ZnO nanowires and Fig. 5.6(b) shows the corresponding Fourier-transformed amplitude spectra. Experimentally obtained frequency dependent refractive index (n_r) and power absorption (α) are extended in the THz region from 0.3 to 3.5 THz.

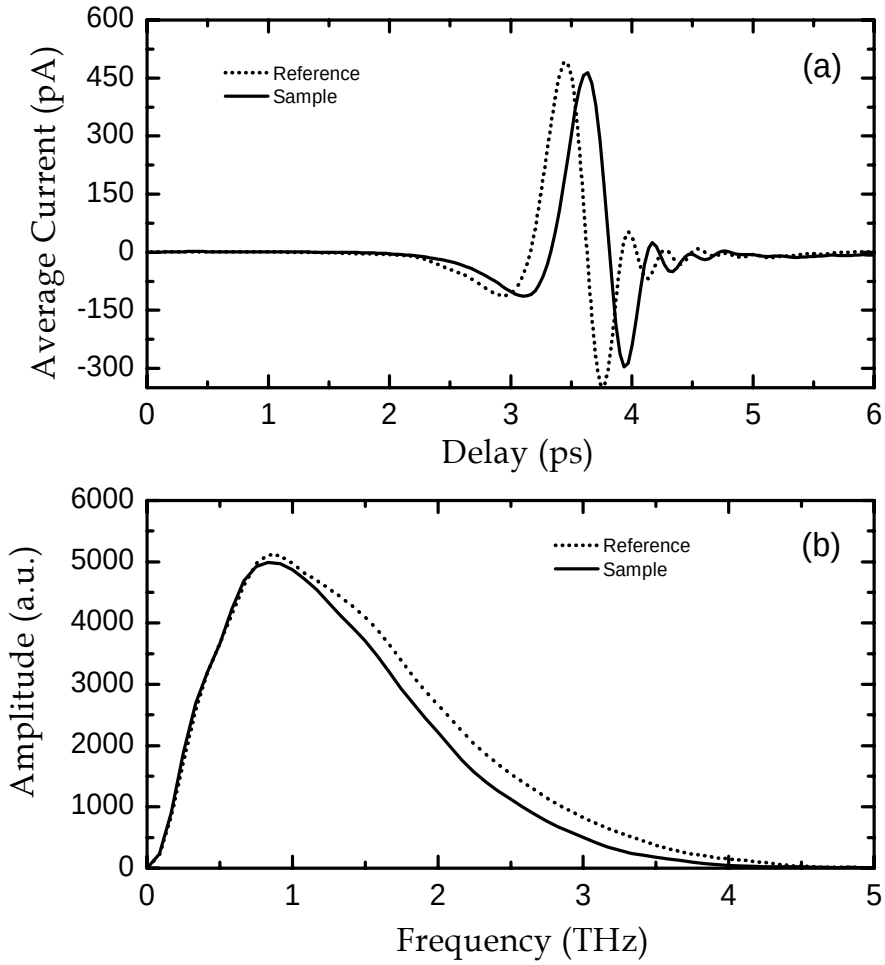

FIG. 5.7 (a) Measured reference and sample pulses and (b) the corresponding Fourier-transformed spectra of ZnO nanowires.

The power absorption and refractive index were extrapolated. The ratio between the amplitude spectra of the reference and that of the sample gave the effective absorption by the sample whereas the phase shift was calculated to determine the refractive index [30]. The frequency-dependent power absorption coefficient $\alpha(\omega)$ and the refractive index $n(\omega)$ are plotted as solid circles in Fig. 5.7. The measured power absorption increases as a function of frequency and no prominent absorption peak is observed below 3.5 THz, whereas the refractive index approaches a constant 1.088.

In the experimental setup the sample was placed in a host medium which plays a significant role. To take this into account we introduce a simple EMT which is described in details in section 4.1. In this EMT theory, f is the filling factor which is defined as the ratio of the volume of actually measured sample to the volume of the cell that held it. The ε_m term present in the above EMT equation is estimated by a pseudo-harmonic equation described within the frame of classical theory which is given by the equation 5.1 which is further reduced and simplified to equation 5.2 by the same way as described above for the ZnO tetrapods. Thus simple effective medium theory in conjunction with the classical theory of independent pseudo-harmonic approximation allows us to obtain a theoretical fit for the calculated refractive index and the power absorption. The procedure followed to calculate the theoretical value of the refractive index and power absorption is described in section 4.1 and *Appendix C*. The refractive index and the power absorption fitting with solid lines is shown below in Fig 5.7. Based on Eq. (5.2), the dotted curves in Fig.5.7 presents a good fit on the experimental data (solid circles) of single crystalline ZnO

nanowire using the parameters: $\varepsilon_\infty = 1.75$, $\varepsilon_{st} = 1.42$, $\omega_{TO}/2\pi = 12.41 \pm 0.2$ THz and $\Gamma/2\pi = 12.50 \pm 0.2$ THz.

The complex dielectric constant is calculated from the experimentally obtained from the results of refractive index and power absorption data. The complex dielectric constant is given by the following relationship: $\varepsilon(\omega) = (n_r + in_i)^2$, where n_r is the real dielectric constant and n_i is the imaginary dielectric constant whereas $\varepsilon(\omega)$ being the complex dielectric constant. The imaginary part of the refractive index is related to the power absorption by the relation, $n_i = \alpha\lambda_0/4\pi$ and therefore the real and imaginary part of the dielectric constant are obtained by the relations: $\varepsilon_r = n_r^2 - (\alpha\lambda_0/4\pi)^2$ and $\varepsilon_i = \alpha n_r \lambda_0/2\pi$ where ε_r and ε_i are real and imaginary dielectric constants [18].

The real and imaginary dielectric constants are shown below in Fig 5.8 and are represented by solid circles. By combining the simplified equation 5.2 and the effective medium theory equation we obtain a theoretical fit for the experimentally obtained real and imaginary dielectric constants by using the same parameters used to obtain the theoretical filling for the refractive index and power absorption. In figure 5.8, the solid lines which represent the theoretical fit for the experimentally obtained dielectric values. The value of the filling factor f used to fit all the refractive index, absorption, and complex dielectric is 0.082. A procedure to obtain the theoretical value of the real and imaginary dielectric constant is described in section 4.3 and Appendix A.

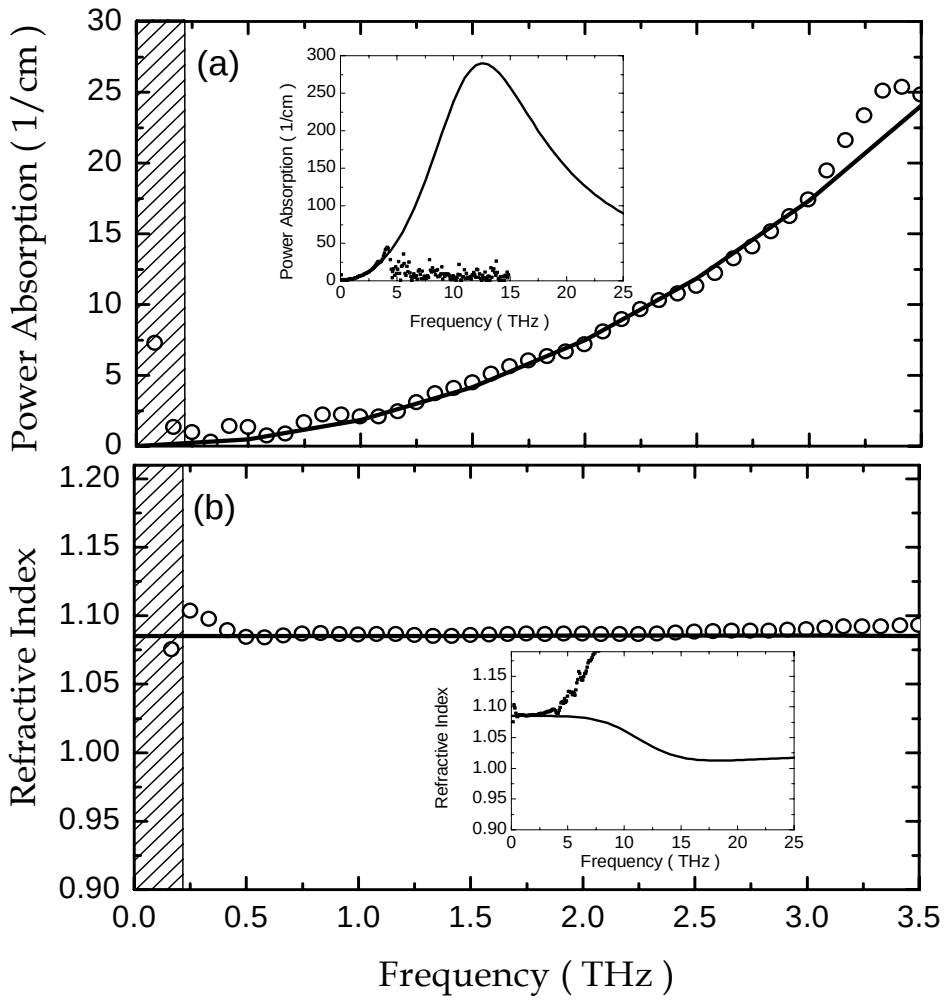

Figure 5.8 (a) Measured refractive (open circles) and theoretical fitting (solid lines) of ZnO nanowires. (b) Measure power absorption of dielectric constant (open circles) and theoretical fitting (solid lines) of ZnO nanowires. . (Inset shows the same curves up to 25 THz).

The fitting reveals the presence of a dominant TO-phonon resonance of ZnO, nanowires, centered at $\omega_{TO}/2\pi = 12.41 \pm 0.2$ THz with a phonon damping constant $\Gamma/2\pi$ = 12.50 ± 0.2 THz and a strength $\varepsilon_{st} = 1.42$.

It can be noted that the TO mode at 12.41 THz is a transverse optical mode in the bulk ZnO of the wurtzite structure with the assignment E_1(TO) [31] If τ is the TO phonon lifetime we have $\tau = 1/\Gamma$ with value $\tau/2\pi$ = 142.85 fs. Actually, τ depends very critically on the type of phonon scattering mechanism and different scattering laws usually define the various lifetimes. The obtained TO phonon lifetime τ results mainly from the calculation of absorption in which scattering from transverse optical phonon has been considered [16].

Like what we have seen in the case of ZnO tatrapods, here also when the radius of the nanostructures tends to approach the Bohr radius of the exciton, the quantum confinement effect will become predominant and noticeable. The dimensions of the tubular sample are ~ 450 nm in diameter and ~ 4 μm in length which are much larger than that of the Bohr radius of ZnO (the calculated value is about 2 nm). This is why no obvious distinctions were observed in dielectric properties between the single-crystal ZnO and nanowire structures [34].

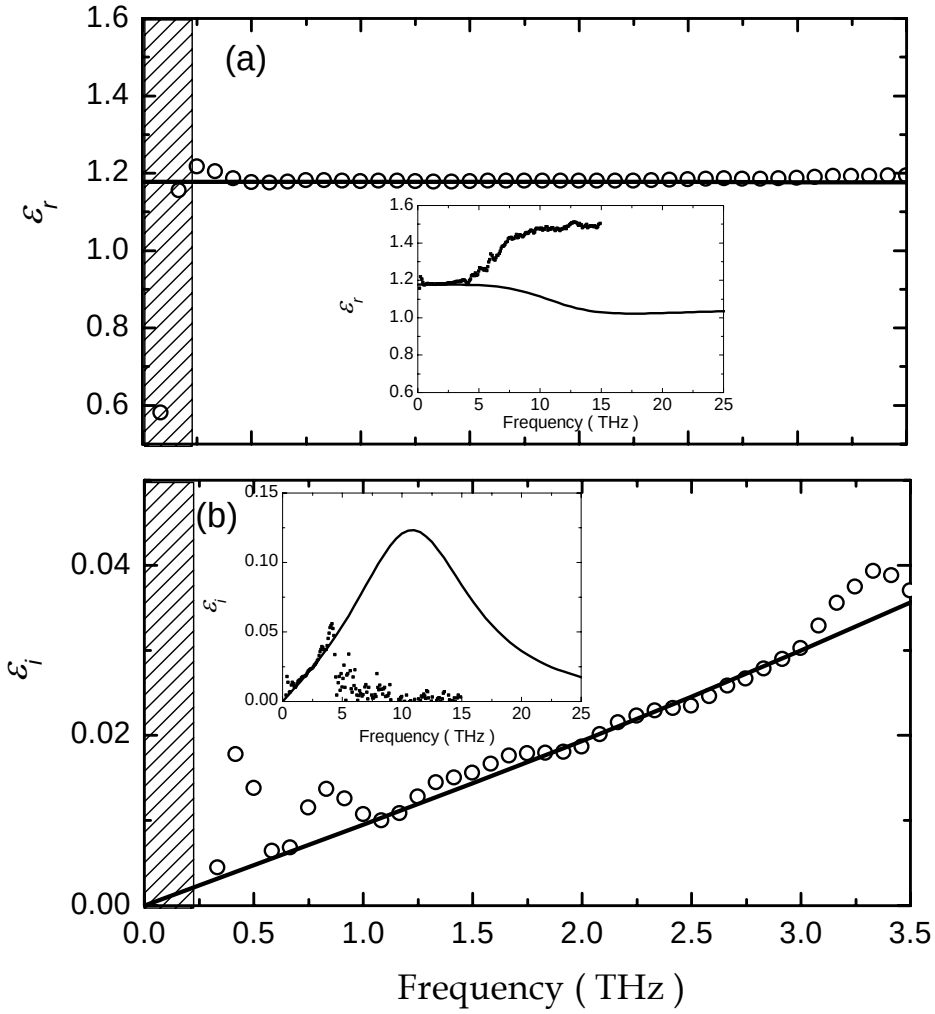

Figure 5.9 (a) Measured real part of dielectric constant (open circles) and theoretical fitting (solid line) of ZnO nanowires (b) Measured imaginary part of dielectric constant (open circles) and theoretical fitting (solid line) of nanowires.(Inset shows the same curves up to 25 THz).

5.9 Comparison between ZnO tetrapods and nanowires

Finally a comparative study of the absorption and the refractive indexes of the ZnO tetrapods and nanowires are shown below in Fig. 5.10. As described earlier both the structures are analyzed by same process and also same procedure was followed to obtain the theoretical fits. This result clearly indicates that both the structures are quite similar in characteristics in the low frequency of the THz regime.

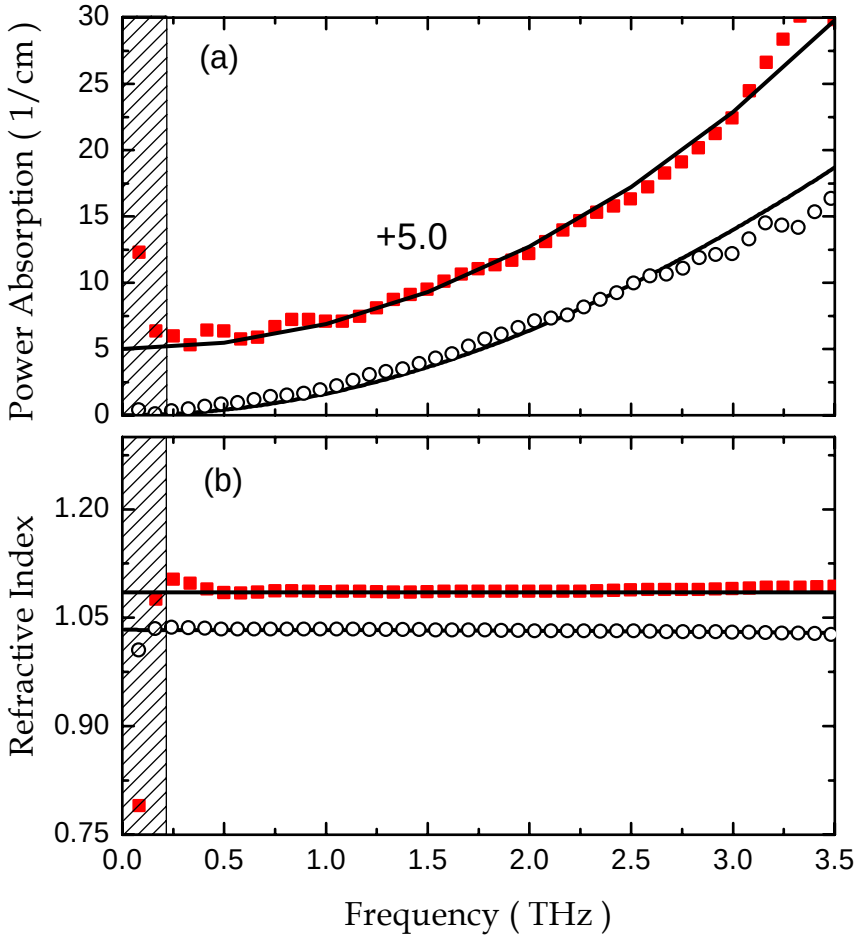

FIG. 5.10 Comparison of (a) measured power absorption (offset by 5.0 1/cm) and (b) refractive index of ZnO tetrapods (open circles) with that of ZnO nanowires (solid squares). The solid curves are the corresponding theoretical fit.

5.10 Theoretical relation of Power absorption and frequency

In the Fig. 5.11 below, a theoretical plot of $\alpha(\omega)$, the power absorption and frequency of the ZnO nanostructures has been shown.

We know that:

$$\varepsilon_{effi}(\omega) = \frac{\alpha(\omega) n_r \lambda_0}{2\pi} \tag{5-3}$$

From Eq. (5-3), we can have

$$\alpha(\omega) = \frac{2\pi\varepsilon_{effi}(\omega)}{\lambda_0} \cdot \frac{1}{n_r} \tag{5-4}$$

Now, from the simple effective medium theory, we can have,

$$\varepsilon_{eff}(\omega) = f[\varepsilon_r(\omega) + i\varepsilon_i(\omega)] + (1-f)\varepsilon_h = \varepsilon_{effr}(\omega) + i\varepsilon_{effi}(\omega)$$

Therefore, $\varepsilon_{effr}(\omega) = f\varepsilon_r(\omega) + (1-f)$ and $\varepsilon_{effi}(\omega) = f\varepsilon_i(\omega)$ (5-5)

Now, by substituting the value of $\varepsilon_{effi}(\omega)$ from Eq. (5-5) to Eq. (5-4), we get

$$\alpha(\omega) = \frac{2\pi f\varepsilon_i(\omega)}{\lambda_0} \cdot \frac{1}{n_r} \tag{5-6}$$

The $\varepsilon_i(\omega)$ term in the Eq. (5-6) can be obtained from the classical pseudo-harmonic model used. According to this model we have

$$\varepsilon(\omega) = \varepsilon_\infty + \frac{(\varepsilon_{st})\omega_{TO}^2}{\omega_{TO}^2 - \omega^2 - i\Gamma\omega} \tag{5-7}$$

Multiplying and dividing the second term of the right hand side of Eq. (5-7) by its complex conjugate and expressing the equation as a combination of real and imaginary parts we get as follows:

$$\varepsilon(\omega) = \varepsilon_\infty + \frac{\omega_{TO}^2(\varepsilon_{st})(\omega_{TO}^2 - \omega^2 + i\Gamma\omega)}{(\omega_{TO}^2 - \omega^2 - i\Gamma\omega)(\omega_{TO}^2 - \omega^2 + i\Gamma\omega)}$$

Now separating in the real and imaginary parts, we obtain:

$$\varepsilon(\omega) = \varepsilon_\infty + \frac{\omega_{TO}^2(\varepsilon_{st})(\omega_{TO}^2 - \omega^2)}{(\omega_{TO}^2 - \omega^2)^2 + \Gamma^2\omega^2} + i\frac{\omega_{TO}^2(\varepsilon_{st})\Gamma\omega}{(\omega_{TO}^2 - \omega^2)^2 + \Gamma^2\omega^2} \tag{5-8}$$

Now by comparing equations (A-b) (from Appendix A) and (5-8), we obtain,

$$\varepsilon_r(\omega) = \varepsilon_\infty + \frac{(\varepsilon_{st})(\omega_{TO}^2 - \omega^2)\omega_{TO}^2}{(\omega_{TO}^2 - \omega^2)^2 + \Gamma^2\omega^2} \tag{5-9}$$

$$\varepsilon_i(\omega) = \frac{(\varepsilon_{st})\omega\Gamma\omega_{TO}^2}{(\omega_{TO}^2 - \omega^2)^2 + \Gamma^2\omega^2} \tag{5-10}$$

Now , subsituting this value of $\varepsilon_i(\omega)$ from Eq. (5-10) to Eq. (5-6), we can obtain,

$$\alpha(\omega) = \frac{2\pi f\varepsilon_i(\omega)}{\lambda_0}\cdot\frac{1}{n_r} = \frac{2\pi f}{\lambda_0 n_r}\left[\frac{\varepsilon_{st}\omega\Gamma\omega_{TO}^2}{(\omega_{TO}^2 - \omega^2)^2 + \Gamma^2\omega^2}\right] \tag{5-11}$$

Here we use the relation: $\lambda_0 = c/\nu$ (c being velocity of light and ν being frequency).

Here, the value of n_r is obtained as described in *Appendix C*, which given by:

$$n_r = \frac{\sqrt{2\varepsilon_{effr}(\omega) + 2\sqrt{\varepsilon_{effr}{}^2(\omega) + 4\varepsilon_{effi}{}^2(\omega)}}}{2}$$

where, $\varepsilon_{effr}(\omega) = f\varepsilon_r(\omega) + (1-f)$ and value of $\varepsilon_r(\omega)$ can be obtained form equation (5-9). Hence we can obtain theoretical plot for $\alpha(\omega)$ and frequency which is shown for three different samples in Fig. 5.11. Fig. 5.11 (a) shows the theoretical plot of the absorption and THz frequency ZnO nanowires, while Fig. 5.11 (b) shows the plot that of ZnO tetrapod and Fig. 5.11 (c) shows the plot of single crystal bulk ZnO. Finally in Fig. 5.11 (d), a comparison of all the three sample has been shown in the THz frequency range of 0.1 – 3.5 THz and the inset of Fig. 5.11 (d) shows the comparative absorption plot of all the three sample up to a range of 50 THz. It is to be noted here that same fitting parameters for all the samples has been used to obtain this analytical theoretical plot.

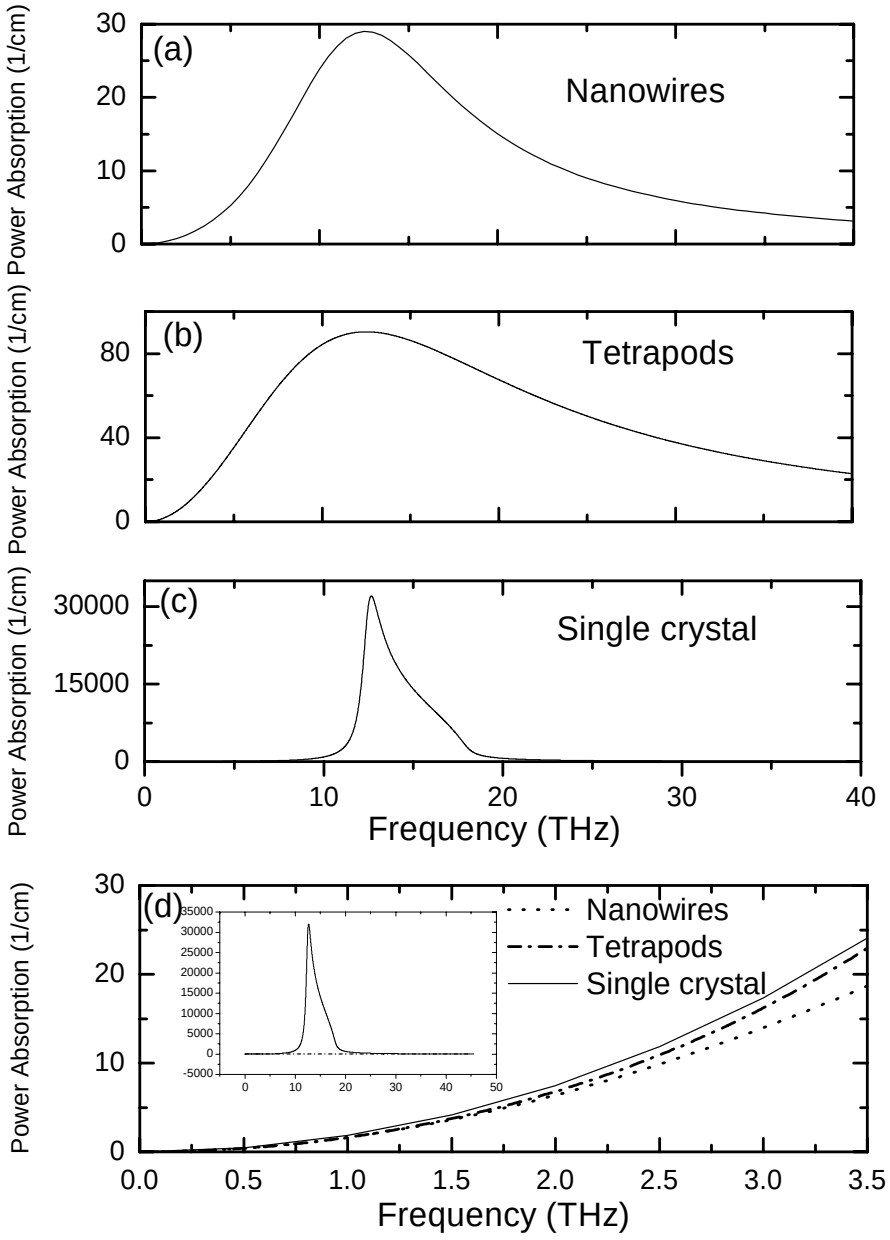

Fig. 5.11. Power absorption of (a) Nanowires (b) Tetrapods and (c) Bulk ZnO and (d) comparison of Nanowires, tetrapods and bulk ZnO up to 3.5 THz and inset show comparison up to 50 THz.

CHAPTER VI

CONCLUSION

This report describes the work which uses a modified THz-TDS system consisting of 8-F confocal geometry, used to characterize different structures of ZnO, a II-VI compound. This specially modified arrangement has four parabolic mirrors carefully placed apart from each other by specific distances that provide a very tight beam with reduced beam diameter in comparison with the 4-F confocal system constituting of two parabolic mirrors. This allows more utilization of the THz power. Our system is perfectly designed and perfectly chosen for this type of work where the sample size is in nanoscale.

The samples characterized in this work are tetrapods and nanowires of ZnO. The frequency-dependent power absorption coefficient $\alpha(\omega)$ and the refractive index $n(\omega)$ are calculated for each sample. The complex dielectric constant is calculated from the experimentally obtained results of refractive index and power absorption data. Thus simple effective medium theory in conjunction with the classical theory of independent pseudo-harmonic approximation allows us to obtain a theoretical fit for the calculated refractive index and the power absorption.

The parameters which where used to obtain the above mentioned fits are: ε_{st}, which is

the oscillator strength, ε_∞, the high frequency dielectric constant, ω_{TO}, the angular frequency of the transverse optical mode and Γ being the damping constant. The filling factor f is also a very important fitting parameter.

The following table summarizes the exact value of the parameters used to fit the index, absorption, real and imaginary dielectric constants of the samples:-

Table I

SAMPLE(ZnO)	ε_{st}	ε_∞	$\omega_{TO}/2\pi$	$\Gamma/2\pi$	f
TETRAPOD	3.40	1.50	12.41 ± 0.2 THz	21.0 ± 0.2 THz	0.01736
NANOWIRE	1.42	1.75	12.41 ± 0.2 THz	12.50 ± 0.2 THz	0.0819334

It shows that the THz spectra of nanostructures of ZnO (tetrapods and nanowires) are dominated by the E_1(TO) phonon mode centered at the frequency 12.41 THz.

Quantum confinement effects are often expected and observed in nanostructures and hence they usually present a quite dissimilar optical property from bulk materials due to their high surface-to-volume ratio or their drastic changes in electron. But our THz-TDS study has shown that the THz spectra of ZnO structures (tetrapods and nanowires) are similar with that of bulk single-crystal ZnO. This implies that the ZnO tetrapods and nanowires preserve almost the overall crystal structure of the bulk ZnO.

CHAPTER VII

FUTURE WORK

In this work, ZnO nanostructures including tatrapods and nanowires have been characterized and analyzed by THz-TDS. As a part of the future work, a more interesting structures (nanobelt, nanorod, nanowall, tube-like and prism like structures) of ZnO can be characterized and compared with bulk crystalline ZnO.

All the structures of ZnO measured here as a part of the thesis work has the dimensions much larger than that of the Bohr radius (which is calculated to be 2 nm) for ZnO. As a part of future work, very fine structures, less than the size of the Bohr radius can be analyzed. This may give some distinctions between the dielectric properties of single-crystal and nanostructured ZnO.

References

1. R. Wu, Y. Yang, S. Cong, Z. Wu, C. Xie, U. Hiroyuki, K. Kawaguchi, and N. Koshizaki, "Fractional dimension and photoluminescence of ZnO tetrapod nanowishkers," Chem. Phys. Lett. **406**, 457 (2005).

2. R. Wu, Y. Yang, S. Cong, J. Kong, and C. Xie, "Optical absorptive characteristics of ZnO tetrapod nanowhiskers," Mater. Lett. **58**, 3792 (2004).

3. W. Zhang, H. Wang, K. S. Wong, Z. K. Tang, G. K. L. Wong, "Third-order optical nonlinearity in ZnO microcrystallite thin films," Appl. Phys. Lett. **75**, 3321 (1999).

4. Z. R. Tian, J. A. Voigt, J. Liu, B. Mckenzie, M. J. McDermott, M. A. Rodriguez, H. Kngishi, and H. Xu, "Complex and Oriented ZnO Nanostructures," Nature Mater. **2**, 821 (2003).

5. Z. K. Tang, G. K. L. Wong, P. Yu, M. Kawasaki, A. Ohtomo, H. Koinuma, and Y. Segawa, "Room-temperature ultraviolet laser emission from self-assembled ZnO microcrystallite thin film," Appl. Phys. Lett. **72**, 3270 (1998).

6. Z. W. Pan, Z. R. Dai, Z. L. Wang, "Nanobelts of Semiconducting Oxides," Science. **291**, 1947 (2001).

7. S. Ono, H. Murakami, A. Quema, G. Diwa, N. Sarukura, R. Nagasaka, Y. Ichikawa, E. Oshima, H. Ogino, A. Yoshikawa, and T. Fukuda, "Generation of THz radiaton from photoconductive switch on zinc oxide single crystal," *in proceedings of CLEO' 2005*, Baltimore, MD, paper CThX6(22-27 May2005)

8. S. Fratini, F. de Pasquale, "Optical absorption from a nondegenerate polaron gas, " Phys. Rev. B **63**, 153101(2001).

9. A. K. Azad, Y. Zhao, W. Zhang, "Transmission properties of terahertz pulses through an ultrathin subwavelength silicon hole array,"Appl. Phys. Lett. **86,** 141102 (2005).

10. L. Thamizhmani, A. K. Azad, J. Dai, and W. Zhang, "Far-infrared optical and dielectric response of ZnS measured by terahertz time-domain spectroscopy," Appl. Phys. Lett. **86**, 131111 (2005).

11. J. M. Dai, J. Zhang, W. Zhang, D. Grischkowsky, "THz time domain spectroscopy (THz-TDS) characterization of the far-infrared absorption and dispersion of high resistivity , float-zone silicon," J. Opt. Soc. Am. B, **21**, 1379-1386 (2004).

12. L. Thamizhmani, "Measurements of the dielectric properties of ZnS in the far infrared using THZ-TDS." Master's Thesis submitted to the faculty of the Graduate college of Oklahoma State University, December, 2004.

13. Mingxia He, Abul K. Azad, Shenghua Ye, Weili Zhang, "Far-infrared signature of animal tissues characterized by terahertz time-domain spectroscopy," Optics Communications, **259**, 389-392 (2006).

14. Orazio Svelto, *Principle of Lasers*, 4th ed. p-148-54 (Plenum Press, New York, 1998).

15. M. Born, and E. Wolf, *Principles of Optics*, 7th (expanded) ed., p. 65, Eq. (58), (Cambridge University Press, Cambridge, UK, 2002).

16. M. Balkanski, in *Optical Properties of Solids*, edited by F. Abeles Chap3, (North- Holland, New york 1972).

17. Abul K. Azad, Jiaguang Han, Weili. Zhang, "Terahertz dielectric properties of high-resistivity single-crystal ZnO," Appl. Phys. Lett. **88** ,021103 (2006).

18. J. G. Han, W. Zhang, W. Chen, L. Thamizhmani, A. K. Azad, Z. Y. Zhu, "Far-infrared characteristics of ZnS nanoparticles measured by terahertz time-domain spectroscopy," Journal of physical Chemistry. B **110**,1989-1993(2006).

19. Jianguang Han, Zhiyuan Zhu, Sanith Ray, Abul K. Azad, Weili Zhang, Mingxia He, Shihong Li, Yiping Zhao, "Optical and dielectric properties of ZnO tetrapod structures at terahertz frequencies," Appl. Phys. Lett. **89** ,031107 (2006).

20. H.-Ch. Weissker, J. Furthmuller, F. Bechstedt, "Validity of effective-medium theory for optical properties of embedded nanocrystallites from *ab initio* supercell calculations," Phys. Rev. B **67**,165322 (2003).

21. H.-Ch. Weissker, J. Furthmuller, F. Bechstedt, "Optical properties of Ge and Si nanocrystallites from *ab initio* calculations. II. Hydrogenated nanocrystallites," Phys. Rev. B **65**,155328 (2002)

22. X.C. Zeng, D. J. Bergman, P. M. Hui, D. Stround, "Effective-Medium Theory for weakly nonlinear composites," Phys. Rev. B **38**, 10970 (1988).

23. J. K. Song, J. M. Szarko, S. R. Leone, S. Li, and Y. Zhao, "Ultrafast Wavelength-Dependent Lasing-Time Dynamics in Single ZnO Nanotetrapod and Nanowire Lasers," J. Phys. Chem. B **109**, 15749 (2005).

24. J. M. Szarko, J. K. Song, C. W. Blackledge, I. Swart, S. R. Leone, S.-H. Li, and Y.-P. Zhao, "Optical injection probing of single ZnO tetrapod lasers**,"** Chem Phys. Lett. **404**, 171 (2005).

25. X. Chu, D. Jiang, A. B. Djurišić, and H. Y. Leung, "Gas-sensing properties of thick film based on ZnO nano-tetrapods," Chem Phys. Lett. **401**, 426 (2005).

26. R. Wu, J. Wu, C. Xie, X. Zhang, and A. Wang, " Morphological characteristic of Zn/ZnO nanopowders and the optical properties," Mater. Sci. Eng. A **328**, 196 (2002).

27. V. A. L. Roy, A. B. Djurišić, H. Liu, X. X. Zhang, Y. H. Leung, M. H. Xie, J. Gao, H. F. Lui, and C. Surya, "Magnetic properties of Mn doped ZnO tetrapod structures," Appl. Phys. Lett. **84**, 756 (2004).

28. Z. Chen, Z. Shan, M. S. Cao, L. Lu, and S. X. Mao, "ZnO Nanotetrapods," Nanotechnology **15**, 365 (2004).

29. Y. H. Leung, A. B. Djurisic, J. Gao, M. H. Xie, and W. K. Chan, "Changing the shape of ZnO nanostructures by controlling Zn vapor release: from tetrapod to bone-like nanorods," Chem. Phys. Lett. **385**, 155 (2004).

30. W. Zhang, A. K. Azad, and D. Grischkowsky, "Terahertz studies of carrier dynamics and dielectric response of *n*-type, freestanding epitaxial GaN," Appl. Phys. Lett. **82**, 2841 (2003).

31. C. A. Arguello, D. L. Rousseau, and S. P. S. Porto, "First-Order Raman Effect in Wurtzite-Type Crystals," Phys. Rev. **181**, 1351 (1969).

32. M. Balkanski, in *Optical Properties of Solids*, edited by F.Abelès, Chap. 8, (North-Holland, New York, 1972).

33. M. Rajalakshmi, A. K. Arora, B. S. Bendre, and S. Mahamuni, "Optical phonon confinement in zinc oxide nanoparticles," J. Appl. Phys. **87**, 2445 (2000).

34. Y. J. Xing, Z. H. Xi, Z. Q. Xue, X. D. Zhang, J. H. Song, R. M. Wang, J. Xu, Y.

Song, S. L. Zhang, and D. P. Yu, "Optical properties of the ZnO nanotubes synthesized via vapor phase growth," Appl. Phys. Lett. **83**, 1689 (2003).

35. J. Zhang, L.D. Sun, H.Y. Pan, et al, "ZnO nanowires fabricated by a convenient route," New Journal of Chemistry **26** (1): 33-34, (2002).

APPENDIXES:

APPENDIX A:

We have the equations.

$$\varepsilon(\omega) = \varepsilon_\infty + \frac{(\varepsilon_0 - \varepsilon_\infty)\omega_{TO}^2}{\omega_{TO}^2 - \omega^2 - i\Gamma\omega} \qquad \textit{(A-a)}$$

$$\varepsilon(\omega) = \varepsilon_r(\omega) + i\varepsilon_i(\omega) \qquad \textit{(A-b)}$$

Multiplying and dividing the second term of the right hand side of equation *(a)* by its complex conjugate and expressing the equation as a combination of real and imaginary parts we gets as follows:

$$\varepsilon(\omega) = \varepsilon_\infty + \frac{\omega_{TO}^2(\varepsilon_o - \varepsilon_\infty)(\omega_{TO}^2 - \omega^2 + i\Gamma\omega)}{(\omega_{TO}^2 - \omega^2 - i\Gamma\omega)(\omega_{TO}^2 - \omega^2 + i\Gamma\omega)} \qquad \textit{(A-c)}$$

Now separating in the real and imaginary parts, we obtain:

$$\varepsilon(\omega) = \varepsilon_\infty + \frac{\omega_{TO}^2(\varepsilon_0 - \varepsilon_\infty)(\omega_{TO}^2 - \omega^2)}{(\omega_{TO}^2 - \omega^2)^2 + \Gamma^2\omega^2} + i\frac{\omega_{TO}^2(\varepsilon_0 - \varepsilon_\infty)\Gamma\omega}{(\omega_{TO}^2 - \omega^2)^2 + \Gamma^2\omega^2} \qquad \textit{(A-d)}$$

Now by comparing equation *(b)* and *(d),* we obtain,

$$\varepsilon_r(\omega) = \varepsilon_\infty + \frac{(\varepsilon_0 - \varepsilon_\infty)(\omega_{TO}^2 - \omega^2)\omega_{TO}^2}{(\omega_{TO}^2 - \omega^2)^2 + \Gamma^2\omega^2} \qquad \textit{(A-e)}$$

$$\varepsilon_i(\omega) = \frac{(\varepsilon_0 - \varepsilon_\infty)\omega\Gamma\omega_{TO}^2}{\omega_{TO}^2 - \omega^2)^2 + \Gamma^2\omega^2} \qquad \textit{(A-f)}$$

APPENDIX B:

We know the following relation:

$$\varepsilon_{eff}(\omega) = f\varepsilon_m(\omega) + (1-f)\varepsilon_h = \varepsilon_{effr}(\omega) + i\varepsilon_{effi}(\omega) \qquad \textit{(B-a)}$$

In the above equation, ε_m is the dielectric constant of the material which can be further splitted into its corresponding real and imaginary parts as:

$$\varepsilon_m(\omega) = \varepsilon_r(\omega) + i\varepsilon_i(\omega) \qquad \textit{(B-b)}$$

Now equation *(B-a)* becomes

$$\varepsilon_{eff}(\omega) = f[\varepsilon_r(\omega) + i\varepsilon_i(\omega)] + (1-f)\varepsilon_h = \varepsilon_{effr}(\omega) + \varepsilon_{effi}(\omega)$$

$$\Rightarrow [f\varepsilon_r(\omega) + (1-f)] + if\varepsilon_i(\omega) = \varepsilon_{effr}(\omega) + i\varepsilon_{effi}(\omega) \qquad \textit{(B-c)}$$

Therefore, we get by comparing the right and left hand side of the equation *(B-c)*

$$\varepsilon_{effr}(\omega) = f\varepsilon_r(\omega) + (1-f) \qquad \textit{(B-d)}$$

$$\varepsilon_{effi}(\omega) = f\varepsilon_i(\omega) \qquad \textit{(B-e)}$$

APPENDIX C:

We have two equations**:-**

$$\varepsilon_{effr}(\omega) = {n_r}^2 - \left(\frac{\alpha\lambda_0}{4\pi}\right)^2 \qquad \textit{(C-a)}$$

$$\varepsilon_{effi}(\omega) = \frac{\alpha n_r \lambda_0}{2\pi} \qquad \textit{(C-b)}$$

From (*C-b*) $\dfrac{\alpha\lambda_0}{2\pi} = \dfrac{\varepsilon_{effi}(\omega)}{n_r}$

Substituting in equation (*C-b*) in (*C-a*) we get,

$$\left(\frac{\varepsilon_{effi}(\omega)}{n_r}\right)^2 = {n_r}^2 - \varepsilon_{eff}(r)$$

$$\Rightarrow {n_r}^4 - {n_r}^2\varepsilon_{effr}(\omega) - {\varepsilon_{effi}}^2(\omega) = 0 \qquad (C\text{-}c)$$

Solving the equation (*C-c*) , we obtain,

$$\therefore n_r = \frac{\sqrt{2\varepsilon_{effr}(\omega) + 2\sqrt{{\varepsilon_{effr}}^2(\omega) + 4{\varepsilon_{effi}}^2(\omega)}}}{2}, -\frac{\sqrt{2\varepsilon_{effr}(\omega) + 2\sqrt{{\varepsilon_{effr}}^2(\omega) + 4{\varepsilon_{effi}}^2(\omega)}}}{2},$$
$$\frac{\sqrt{2\varepsilon_{effr}(\omega) - 2\sqrt{{\varepsilon_{effr}}^2(\omega) + 4{\varepsilon_{effi}}^2(\omega)}}}{2}, -\frac{\sqrt{2\varepsilon_{effr}(\omega) - 2\sqrt{{\varepsilon_{effr}}^2(\omega) + 4{\varepsilon_{effi}}^2(\omega)}}}{2} \qquad (C\text{-}d)$$

The first set of result in the above equation is used to obtain the value of n_r while other sets are discarded.

From (*C-b*), we can obtain $\alpha = \dfrac{2\pi\varepsilon_{effi}(\omega)}{\lambda_0} \cdot \dfrac{1}{n_r}$ $(C\text{-}e)$

Note : The value of $\varepsilon_{eff}(r)$ and $\varepsilon_{eff}(i)$ used here are obtained by the method as described in *Appendix B*.

VITA

Sanith Ray

Candidate for the Degree of

Master of Science

Thesis: OPTICAL AND DIELECTRIC PROPERTIES OF ZnO NANOSTRUCTURES AT TERAHERTZ FREQUENCIES

Major Field: Electrical Engineering

Biographical:

Education: Graduated from Sikkim Manipal Institute of Technology in May 2001; received Bachelor of Engineering degree in Electronics and communication. Completed the requirements for the Master of Science degree with a major in Electrical Engineering at Oklahoma State University in May 2006.

Professional Experience: Graduate Research Assistant, School of Electrical and Computer Engineering, Oklahoma State University, May 2005 to July 2005. Computer Support team in Oklahoma EPSCoR from August 2005 to resent. Teaching assistant from January 2005 to May 2005, School of Electrical and computer Engineering, Oklahoma State

Name: Sanith Ray **Date of Degree**: May, 2006

Institution: Oklahoma State University **Location:** Stillwater, Oklahoma

Title of Study: OPTICAL AND DIELECTRIC PROPERTIES OF ZnO NANOSTRUCTURES AT TERAHERTZ FREQUENCIES

Pages in Study: 67 Candidate for the degree of Master of Science

Major Field: Electrical Engineering

Scope and Method of Study: The purpose of this study is to characterize the optical and dielectric properties of the nanostructures of ZnO in the far infrared regime using THz time-domain spectroscopy. The experimentally obtained frequency dependent refractive indices, power absorptions and complex dielectric constants for nanowires and tetrapods were theoretically fit by using a simple mixing model in tandem with classical pseudo-harmonic model.

Findings and Conclusion: The experimentally obtained results of refractive indices, power absorption coefficients and complex dielectric functions fit well using the theoretical approach. The fitting revealed the presence of dominant TO-phonon mode centered at 12.41 THz for both the samples. Very similar THz spectra of the characterized nanostructures with that of the bulk allowed us to conclude that these nanostructures have similar crystal structure of bulk ZnO.